

# An evaluation of machine learning/molecular mechanics end-state corrections with mechanical embedding to calculate relative protein–ligand binding free energies

Johannes Karwounopoulos<sup>#</sup>, Mateusz Bieniek<sup>#</sup>, Zhiyi Wu, Adam L. Baskerville, Gerhard König,<sup>\*</sup> Benjamin P. Cossins, and Geoffrey P. F. Wood

*Exscientia, Schrödinger Building, Oxford Science Park, Oxford, UK*

E-mail: gkoenig@exscientia.co.uk

## Abstract

The development of machine-learning (ML) potentials offers significant accuracy improvements compared to molecular mechanics (MM) because of the inclusion of quantum-mechanical effects in molecular interactions. However, ML simulations are several times more computationally demanding than MM simulations, so there is a trade-off between speed and accuracy. One possible compromise are hybrid machine learning/molecular mechanics (ML/MM) approaches with mechanical embedding that treat the intramolecular interactions of the ligand at the ML level and the protein-ligand interactions at the MM level. Recent studies have reported improved protein-ligand binding free energy results based on ML/MM with mechanical embedding, arguing that intramolecular interactions like torsion potentials of the ligand are often the limiting factor for accuracy. This claim is evaluated based on 108 relative binding free

---

<sup>#</sup>Contributed equally

energy calculations for four different benchmark systems. As an alternative strategy, we also tested a tool that fits the MM dihedral potentials to the ML level of theory. Overall, the relative binding free energy results from MM with Open Force Field 2.2.0, MM with ML-fitted torsion potentials, and the corresponding ML/MM end-state corrected simulations show no statistically significant differences in the mean absolute errors (between 0.8 and 0.9 kcal mol<sup>-1</sup>). This can probably be explained by the usage of the same MM parameters to calculate the protein-ligand interactions. Therefore, a well-parameterized force field is on a par with simple mechanical embedding ML/MM simulations for protein-ligand binding. In terms of computational costs, the reparametrization of poor torsional potentials is preferable over employing computationally intensive ML/MM simulations of protein-ligand complexes with mechanical embedding. Also, the refitting strategy leads to lower variances of the protein-ligand binding free energy results than the ML/MM end-state corrections. For free energy corrections with ML/MM, the results indicate that better convergence and more advanced ML/MM schemes will be required for applications in computer-guided drug discovery.

## 1 Introduction

Relative binding free energy (RBFE) calculations have become a standard tool in computational drug discovery,<sup>1-5</sup> where rigorous physics-based predictions of protein-ligand binding serve both to enrich the number of active compounds for experimental testing,<sup>6-9</sup> and to provide machine-learning drug-discovery pipelines with additional data.<sup>10</sup> Nowadays, RBFE calculations typically yield root mean square errors between 0.4 and 4.3 kcal mol<sup>-1</sup> relative to experimental protein-ligand binding affinities,<sup>11-13</sup> depending on the quality of the underlying protein structure, sampling, and force field.<sup>14</sup>

A major challenge for RBFE calculations in computational drug discovery is the accurate description of molecular interactions from the vast space of drug-like chemical compounds.

Uncommon chemical groups might not be well-supported by force fields, which can lead to large errors. Two possible strategies to address this problem are a) the reparametrization of the force field based on quantum-mechanical (QM) calculations, or b) using a hybrid quantum mechanics/molecular mechanics (QM/MM) approach to describe the ligand.<sup>15-19</sup> One of the most simple QM/MM techniques is mechanical embedding, where the intramolecular interactions of the ligand are treated at the QM level, while the environment and the ligand-environment interactions are calculated at the MM level. Unfortunately, it is rarely possible to perform free energy calculations directly at the QM level of theory,<sup>20-22</sup> because of the high computational demands and the need to implement dummy atoms and soft core potentials for alchemical transformations. To address these challenges, indirect free energy methods that employ end-state corrections have been developed.<sup>15-19,22-35</sup> Instead of performing the entire alchemical transformation at the QM level, the free energy difference is first calculated at the MM level. Then, the free energy differences between the MM and the QM energy surfaces are computed and added as correction terms to the MM free energy difference. For the RBFE between two ligands A and B at the QM level of theory ( $\Delta\Delta G_{A\rightarrow B}^{\text{QM}}$ ), this corresponds to:

$$\Delta\Delta G_{A\rightarrow B}^{\text{QM}} = \Delta\Delta G_{A\rightarrow B}^{\text{MM}} - \Delta G_A^{\text{MM}\rightarrow\text{QM}} + \Delta G_B^{\text{MM}\rightarrow\text{QM}} \quad (1)$$

Here,  $\Delta\Delta G_{A\rightarrow B}^{\text{MM}}$  is the RBFE between two ligands at the MM level of theory, while  $\Delta G_A^{\text{MM}\rightarrow\text{QM}}$  and  $\Delta G_B^{\text{MM}\rightarrow\text{QM}}$  are the end-state corrections from MM to QM for each ligand. In several instances, free energy calculations with QM has substantially improved the accuracy of the results under blind conditions.<sup>8,28,32,34,36</sup>

The main challenge of end-state corrections is the convergence of free energy calculations between the MM and QM.<sup>37</sup> If the MM energy surface is not representative of the QM energy surface, most of the MM sampling is conducted in regions of phase space that have a very low probability in QM, which lowers the number of effective samples. In many cases, the stiffest degrees of freedom in MM, the bond lengths and angles, slightly differ from the QM level of choice.<sup>38-40</sup> To resolve this convergence issue, reparametrization techniques<sup>38-42</sup> and

nonequilibrium switching (NEQ) methods<sup>43,44</sup> can be employed.

ML approaches trained on QM data have recently been shown to reliably reproduce QM potential energy surfaces, striking a balance between accuracy and speed.<sup>45,46</sup> A prominent example for such ML approaches is the ANI family of neural network potentials, with ANI-2x being particularly popular for tasks like conformer generation and chemical property prediction.<sup>47-51</sup> ANI-2x was trained with an active learning strategy on 8.9 million molecular conformations, using the  $\omega$ B97X/6-31G\* level of theory. Recently, the use of ANI-2x has been reported for protein-ligand binding calculations using RBF simulation<sup>52,53</sup> and the linear interaction energy method.<sup>54</sup> Refs. 52 and 53 employed an indirect free energy cycle with end-state corrections,<sup>55</sup> where the ANI-2x potential served as the QM potential to correct free energies calculated at the MM level. A similar end-state correction approach was also recently used to calculate hydration free energies.<sup>56</sup> Therefore, the employment of ML/MM approaches instead of QM/MM approaches to calculate free energy differences is an attractive choice.

Another possible strategy to employ ML potentials to improve the reliability of protein-ligand binding predictions for diverse chemical spaces is the reparametrization of existing force fields.<sup>38-41,57</sup> This approach has also been termed bespoke parametrization,<sup>42,57</sup> or tuned force fields. A recent report indicates that tuned force fields can be on a par with ML/MM simulations in terms of energies and conformational sampling,<sup>58</sup> which makes the reparametrization approach attractive, as MM simulations are computationally less demanding than ML/MM simulations. Results for drug-like molecules show that the ANI-ML potentials are capable of closely reproducing the underlying QM torsional potential energy surfaces,<sup>59</sup> which indicates that ML calculations could be employed for the fitting of torsion potentials in an automated computational drug discovery pipeline.

Here, both ML potentials for the reparametrization of force fields and the use of end-state corrections based on ML/MM simulations with ANI-2x are evaluated for the calculation of RBF simulation of protein-ligand systems in drug discovery. Four benchmark systems TYK2,<sup>60,61</sup>

CDK2,<sup>62</sup> JNK1,<sup>63</sup> and P38<sup>64</sup> from Ref. 65 are employed for to test the accuracy of the methods based on 108 RBFEE results. In the following sections, the methodological details of the RBFEE calculations with MM, the torsion potential fitting with the in-house Torpenter tool, and the end-state corrections are described. Following this, the RBFEE protocols are verified based on reported results in the literature. The effect of the parameter refitting with ML and end-state corrections with ML/MM are discussed based on the mean absolute errors of the RBFEE results. Finally, a set of recommendations and guidelines are laid out.

## 2 Methods

### 2.1 Relative binding free energy calculations

RBFEE calculations were conducted for 108 ligand pairs of the benchmark systems TYK2, CDK2, JNK1, and P38.<sup>65</sup> Four ligands had to be removed because the ANI-2x model is not parameterized for Br (ligand 17 in CDK2, and ligands 17124.1 and 18636.1 of JNK1) or charged molecules (ligand 18639.1 in JNK1). The RBFEE calculations employed the standard thermodynamic cycles,<sup>66</sup> which involve free energy simulations of the protein-ligand complex (bound leg) and the ligand in solution (free leg). Ligand mappings were generated with the in-house `Pertmapper` tool,<sup>67</sup> and the ligand network was constructed with `LOMAP`.<sup>68</sup> Alchemical transformations were prepared according to the recommendations by Fleck, Wieder, and Boresch,<sup>69</sup> using an in-house strain removal algorithm. The end states were equilibrated separately using the robust protocol of Roe and Brooks.<sup>70</sup> The alchemical system was divided into 12  $\lambda$ -windows: the first six windows were started from the equilibration of the initial state ( $\lambda = 0$ ) and the final six windows from the structure of the final state ( $\lambda = 1$ ). For each  $\lambda$ -state, the energy was minimized with 100 steps of steepest descent. This was followed by another equilibration phase of 0.04 ns with a 1 fs timestep at 298 K, utilizing the Langevin integrator and a Monte Carlo barostat set to 1 atm.<sup>71</sup> The production run lasted 2 ns with a 2 fs timestep, using Hamiltonian replica exchange with an interval of 2 ps

to enhance sampling.<sup>72,73</sup> Free energy data were analyzed using Alchemlyb and the UBAR solver inspired by Giese and York.<sup>74</sup>

## 2.2 Torsion potential refitting with Torpenter

Torpenter (short for “Torsion Carpenter”) is a package for refitting the torsion potentials in a molecule according to QM or ML calculations, analogously to the `BespokeFit` and `QubeKit` packages.<sup>42,57</sup> First, the torsion profile is created by scanning the torsions. For this, the `TorsionDrive` package<sup>75</sup> is used in combination with `ASE`<sup>76</sup> using the ANI-2x neural network potential.<sup>49</sup> The 1-dimensional torsion scans utilized the step of 15° for each rotatable torsional degree of freedom, as selected according the `OpenMM Fragmenter` tool.<sup>77</sup> Constraints, as implemented in the `FixInternals` tool of `ASE`, are applied to the selected torsion, followed by an energy minimization using the ANI-2x neural network potential in the `ASE` package. Based on the potential energies of the different rotational substates, the `ForceBalance` package<sup>78</sup> is used to create the torsion potential with predetermined defaults. The bespoke force field parameters are then saved as an offxml file for the use in `Open Force Field`.<sup>79</sup>

## 2.3 End-state Corrections

The end-state corrections for the protein-ligand binding free energies were conducted analogously to previous solvation free energy calculations described in Ref. 56. Equilibrium simulations were conducted for both the MM and the ML levels of theory, which then served as starting points for bidirectional nonequilibrium switching simulations to calculate the free energy difference with the Crooks free energy estimator.<sup>80</sup>

For each compound, three independent MM simulations were performed both in aqueous solution and in the bound state using `OpenMM 8.1`<sup>77</sup> either with the `Open Force Field 2.2.0 (OFF2.2.0)`<sup>81</sup> or the Torpenter-derived force field described in the previous section. The molecules were solvated in `TIP3P` water,<sup>82</sup> and the chemical bonds of water were constrained

with the SETTLE algorithm.<sup>83</sup> The simulations were conducted at a temperature of 300 K, using Langevin dynamics with a friction constant of  $1 \text{ ps}^{-1}$ , and a pressure of 1 bar, using a Monte Carlo barostat.<sup>84,85</sup> The time step was 2 fs, using hydrogen mass repartitioning for all non-water hydrogens to set the hydrogen masses to 3 amu. The electrostatic interactions were computed with the particle mesh Ewald method,<sup>86,87</sup> using a short-range cutoff of 10 Å. Before each simulation, the geometry of the solute was optimized using the L-BFGS minimizer, followed by 1 ns of constant volume equilibration. The production simulation with constant pressure was performed for 5 ns, whereof the first nanosecond was employed as equilibration. From the last 4 ns, 300 frames were written using a saving frequency of 12 ps, and used as the starting points for the NEQ switches.

The ML/MM simulations were carried out analogously to the MM simulations, except that the intramolecular interactions of the ligand were modelled with the ANI-2x neural network potential using a mechanical embedding approach as implemented in `OpenMM-ML`.<sup>49,52</sup> Thus, the interactions between the ligand and the environment are still treated at the MM level. The high-performance ANI-2x implementation `NNPOPS` (v.0.6) was used.<sup>88</sup>

300 nonequilibrium (NEQ) switching simulations were started from both the MM and ML/MM trajectories to calculate the free energy difference for the end-state corrections. The NEQ protocol consisted of 5 ps simulations with a 1 fs time step where the energy function is slowly interpolated from one state to the other (either MM→ML, or ML→MM). This was achieved by using the coupling parameter  $\lambda$  to interpolate between the MM and ML/MM potential energy functions according to  $U = (1 - \lambda)U_{\text{MM}} + \lambda U_{\text{ML/MM}}$ , or vice versa. The  $\lambda$  variable was adjusted in an alternating sequence of 1 perturbation and 1 propagation time steps. In each perturbation step, the coupling parameter was adjusted to  $\lambda = t/\tau$ , where  $t$  is the current time step and  $\tau$  the total number of steps of the protocol. The nonequilibrium work value,  $W$ , is updated at each perturbation step using  $W_t = W_{t-1} + U_{t+1}(x_{t+1}) - U_t(x_{t+1})$ . Bennett’s acceptance ratio, as implemented in `pymbar`,<sup>89</sup> was used to calculate the free energy difference from the nonequilibrium work values.

### 3 Results and Discussion

Table 1: Comparison of the mean absolute errors (MAE) of the relative binding free energies and their corresponding standard deviations from error propagation using the Open Force Field 2.2.0 (OFF2.2.0), the refitted force field based on torsion potentials from Torpenter with ANI-2x (TOR), and the corresponding end-state corrected metrics (EC) using ANI-2x. The last row shows the average results over all 108 relative binding free energies. All data are in kcal mol<sup>-1</sup>.

MAE	MM		ML/MM	
	OFF2.2.0	TOR	EC-OFF2.2.0	EC-TOR
TYK2	0.6 ± 0.2	0.7 ± 0.2	0.6 ± 0.9	0.6 ± 0.7
CDK2	0.6 ± 0.5	0.6 ± 0.5	0.6 ± 0.7	0.8 ± 0.6
JNK1	0.5 ± 0.2	0.5 ± 0.2	1.1 ± 1.8	1.0 ± 1.2
P38	1.0 ± 0.5	1.1 ± 0.6	1.0 ± 0.7	1.1 ± 0.7
<b>Average</b>	<b>0.8 ± 0.4</b>	<b>0.8 ± 0.4</b>	<b>0.9 ± 1.1</b>	<b>0.9 ± 0.8</b>

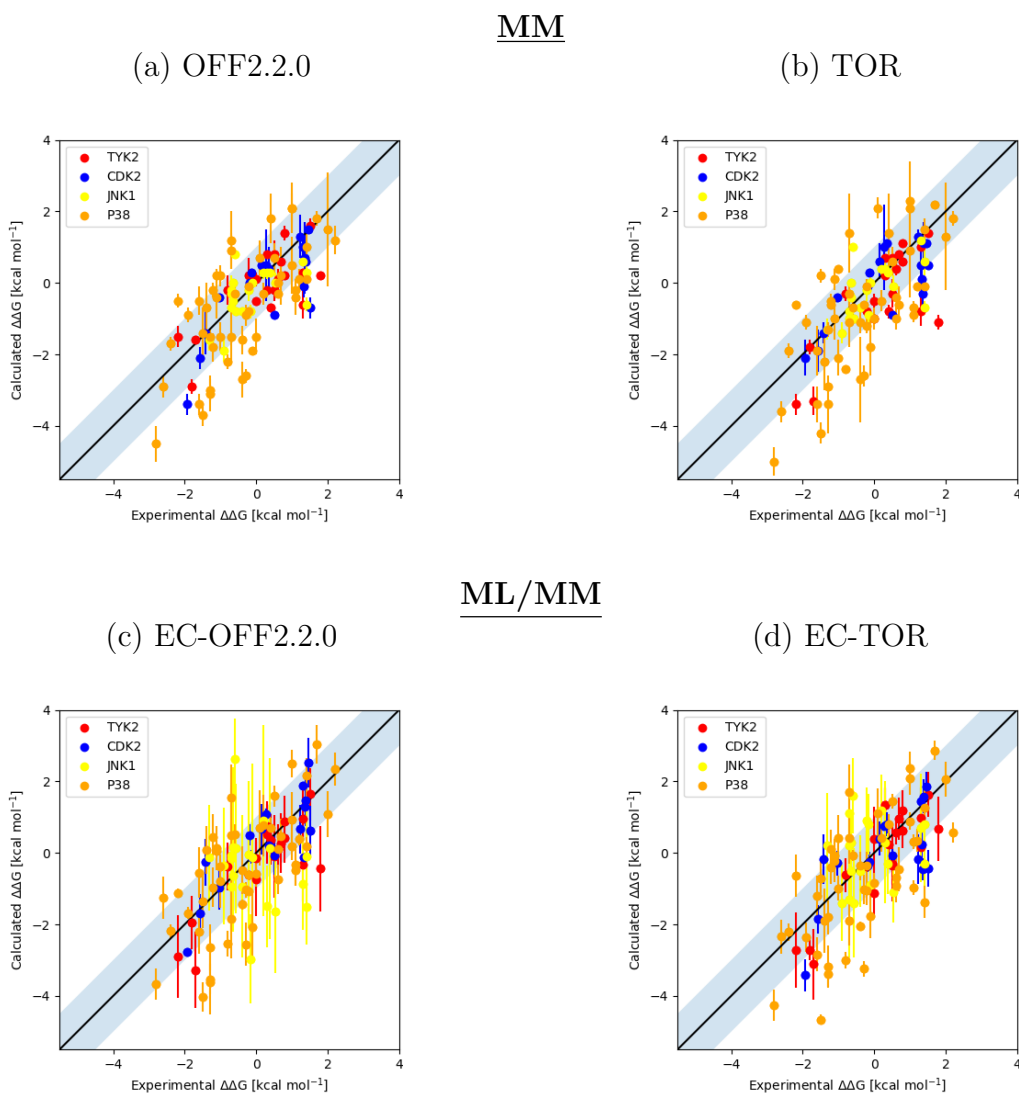
#### 3.1 Verification based on reported binding affinities

As a first step, the underlying protocol for the relative free energy simulations with OFF2.2.0 is validated based on published results. The mean absolute errors (MAE) of OFF2.2.0 with respect to experiment are reported in the first column of Table 1. The corresponding root mean square error (RMSE) and  $R^2$  data are reported in Table S1 in the SI.

Recently published protein-ligand affinity predictions with OFF2.0 by Hahn et al.<sup>11</sup> reported MAE of 1.0 kcal mol<sup>-1</sup> for TYK2 and CDK2, and 0.7 kcal mol<sup>-1</sup> for JNK1 and P38. The MAE from OFF2.2.0 in Table 1 are slightly better for TYK2 (0.6 kcal mol<sup>-1</sup>), CDK2 (0.6 kcal mol<sup>-1</sup>), and JNK1 (0.5 kcal mol<sup>-1</sup>), and slightly worse for P38 (1.0 kcal mol<sup>-1</sup>). Overall, the average MAE of the OFF2.0 results by Hahn et al. for the four systems is 0.8 kcal mol<sup>-1</sup>, which is identical with the average MAE here (0.8 kcal mol<sup>-1</sup>). Thus, the present MM relative binding free energy results agree very well with the results of the longer 6 ns nonequilibrium protocol by Hahn et al.<sup>11</sup>



Figure 1: Comparison of the 108 relative binding free energies  $\Delta\Delta G$  from MM (top) and ML/MM end-state corrections using mechanical embedding (bottom) using Open Force Field 2.2.0 (OFF2.2.0, left), and the refitted force field based on torsion potentials from Torpenter with ANI-2x (TOR, right). The simulated  $\Delta\Delta G$  values (y-axis) are plotted with respect to experiment (x-axis). The error bars correspond to the standard deviations from three repeats. The shaded area highlights deviations below  $1 \text{ kcal mol}^{-1}$ . Overall, the  $\Delta\Delta G$  results from MM and ML/MM with mechanical embedding show a similar level of accuracy, but the ML/MM results exhibit significantly higher random fluctuations.



### 3.2 Effect of torsion fitting with Torpenter

The mean absolute errors (MAE) with respect to experiment of OFF2.2.0 and the refitted parameters from Torpenter (TOR) are reported in the first two columns Table 1. Overall, OFF2.2.0 and TOR yield the same level of accuracy with MAE of  $0.8 \text{ kcal mol}^{-1}$ , as well as the same level of precision with average standard deviations of  $0.4 \text{ kcal mol}^{-1}$ . This is also shown by the plots of the  $\Delta\Delta G$  results in Fig. 1a and Fig. 1b, where OFF2.2.0 and TOR yield very similar results. Interestingly, five data points from P38 (shown in orange) exhibit standard deviations above  $1 \text{ kcal mol}^{-1}$  which are markedly higher than with OFF2.2.0. This suggests that, in some cases, the ML energy surface that was used for the reparametrization of the torsion potentials might be more rugged than the MM energy surface of OFF2.2.0.

A direct comparison of all RBFE from TOR with respect to the corresponding values from OFF2.2.0 yields a mean signed deviation of just  $-0.1 \text{ kcal mol}^{-1}$  and a mean absolute deviation of  $0.4 \text{ kcal mol}^{-1}$ . The mean unsigned deviation between TOR and OFF2.2.0 corresponds to the average standard deviation of the TOR results ( $0.4 \text{ kcal mol}^{-1}$ ), which indicates that the observed differences are most likely the result of random fluctuations. The corresponding RMSE and  $R^2$  data in Table S1 of the Supporting Information also indicate that both methods yield the same level of accuracy and precision. This is quite remarkable, considering that the torsion potentials of the OFF2.2.0 force field were specifically fine-tuned for the compounds in the considered benchmark systems. The results demonstrate that the Torpenter-derived torsion parameters from the fast neural network potential ANI-2x are on a par with the highly optimized parameters based on the B3LYP-D3BJ/DZVP level of theory, which suggests that Torpenter could be used for a fast on-the-fly reparametrization of all rotatable torsions of ligands in an automated drug discovery pipeline.

### 3.3 Effect of ML/MM end-state corrections with mechanical embedding

The two rightmost columns of Table 1 show the mean absolute errors and standard deviations of relative binding free energies that include MM→ML/MM end-state correction based mechanical embedding with ANI-2x. Because of error propagation, the standard deviations include both the uncertainty of the MM results and of the end-state corrections. The variance of the end-state corrections depends on the number and switching speed of the NEQ work calculations,<sup>90</sup> and the phase-space overlap between the MM and ML/MM energy surfaces.<sup>37</sup> For example, previous free energy results based on end-state corrections with QM/MM have reported standard deviations between 0.1 and 2.9 kcal mol<sup>-1</sup> for hydration free energies (with average standard deviations of about 0.6 to 1.0 kcal mol<sup>-1</sup>).<sup>28,38</sup> For transfer free energies between water and cyclohexane, the reported standard deviations lie between 0.4 and 4.4 kcal mol<sup>-1</sup>, with an average of 1.5 kcal mol<sup>-1</sup>,<sup>34</sup> and, for host-guest binding calculations, the range of the standard deviations is between 0.4 and 1.3 kcal mol<sup>-1</sup>.<sup>91</sup> Even when using best practices by employing NEQ switching and the Crooks estimator, the standard deviations of end-state corrections can rise up to 9.7 kcal mol<sup>-1</sup> for challenging molecules in the HiPen database.<sup>92</sup> Thus, while the error bars of the MAE with ML/MM in Table 1 are 1.2 to 9-times higher than the corresponding MM results, they lie well in the range that can be expected for end-state corrections.

Overall, the average MAE with EC from ML/MM with mechanical embedding are 0.9 kcal mol<sup>-1</sup> for both OFF2.2.0 and TOR. Considering that the average standard deviations are 1.1 and 0.9 kcal mol<sup>-1</sup>, respectively, the differences between the MM and ML/MM results with mechanical embedding are not statistically significant. This view is also supported by the comparison of the MM and ML/MM results with mechanical embedding in Fig. 1, where no systematic differences are discernible. A direct comparison of the individual RBF results from EC-OFF2.2.0 and OFF2.2.0 yields a mean unsigned deviation of 0.4 kcal mol<sup>-1</sup> and a mean absolute deviation of 0.6 kcal mol<sup>-1</sup>, which is smaller than the

mean standard deviation of  $1.1\text{kcal mol}^{-1}$  of the EC-OFF2.2.0 results. Likewise, the mean unsigned deviation between EC-TOR and TOR is  $-0.1\text{kcal mol}^{-1}$  and the corresponding mean absolute deviation is  $0.6\text{kcal mol}^{-1}$ , which is smaller than the mean standard deviation of  $0.8\text{kcal mol}^{-1}$  of the EC-TOR results. Thus, any observed improvement or loss of accuracy is likely attributable to random noise.

Focusing on RBFE for the TYK2 benchmark, Ref. 52 reported an MAE of  $0.7\text{kcal mol}^{-1}$  using ML/MM end-state corrections with ANI-2x. The MAE for EC with ANI-2x based on simulations with OFF2.2.0 and TOR in the first row of Table 1 are slightly better with of  $0.6\text{kcal mol}^{-1}$ . Thus, both the MM simulations with OFF2.2.0 and TOR, and the ML/MM simulations with EC with mechanical embedding with ANI-2x and the results from Rufa et al. yield the same level of accuracy for the TYK2 benchmark, considering the uncertainties of the free energy results. The main difference compared to previously reported relative binding free energy calculations in Ref. 52 is that the previous MM simulations with OFF1.0.0 yielded an MAE of  $1.0\text{kcal mol}^{-1}$ , while MM simulations with OFF2.2.0 yield an MAE of  $0.6\text{kcal mol}^{-1}$  (first column of Table 1). The main differences between OFF1.0 and OFF2.0 is the refitting of the Lennard-Jones parameters,<sup>81</sup> which affects both the protein-ligand interactions and the intramolecular interactions of the ligand, as well as the fitting of a series of torsions to QM data.

In Ref. 53, RBFE with ANI-2x and mechanical embedding were calculated with the alchemical transfer method<sup>93</sup> and compared to the GAFF2 force field. Within Ref. 53, the reported MAE of relative binding free energies with ML/MM are  $0.5\text{kcal mol}^{-1}$  for TYK2,  $0.7\text{kcal mol}^{-1}$  for CDK2,  $0.7\text{kcal mol}^{-1}$  for JNK1, and  $0.9\text{kcal mol}^{-1}$  for P38. While the number of alchemical transformations for TYK2, CDK2, JNK1, and P38 in Ref. 53 was 84, which is smaller than the number of transformations in the present study (108), the MAE in Table 1 and in Ref. 53 are very similar, and, overall, the differences are not statistically significant. The average MAE of ML/MM for the four systems TYK2, CDK2, JNK1, and P38 from Ref. 53 is  $0.7\text{kcal mol}^{-1}$ , which is comparable to the results here. The MAE of

MM with the GAFF 2.11 force field from Ref. 53 is  $1.0 \text{ kcal mol}^{-1}$ , which is lower accuracy than the MAE of MM with OFF2.2.0 in Table 1. While the GAFF 2.11 data suggests that mechanical embedding using ANI-2X has an average accuracy improvement of approximately  $0.3 \text{ kcal mol}^{-1}$  over the pure MM simulations, the results in Table 1 suggest a decrease of accuracy by approximately  $0.1 \text{ kcal mol}^{-1}$ . However, due to the high standard deviations of the ML/MM results, the differences are not statistically significant, and any differences might be explained by the underlying force field.

The largest deviations of the end-state corrections are observed for JNK1 using EC-OFF2.2.0, with an MAE of  $1.2 \pm 1.9 \text{ kcal mol}^{-1}$  (third column of Table 1). Only 6 of the 21 RBFE calculations of JNK1 exhibit errors of more than  $1.5 \text{ kcal mol}^{-1}$ , and all of these can be traced back to just two ligands: 18634\_1 and 18628\_1 (Table S4 of the SI). Ligand 18628\_1 is characterized by the addition of a methyl group to the common core, while ligand 18634\_1 involves the addition of two methoxy groups (Fig. S11 in the SI). Given the simplicity of those additions, an error of the force field or ML potential is highly unlikely. Yet, the ML/MM end-state corrections for 18634\_1 and 18628\_1 exhibit some of the largest magnitudes in this benchmark system, with  $3.8$  and  $3.3 \text{ kcal mol}^{-1}$ , respectively. As evidenced by the histograms of the nonequilibrium work between MM and ML/ML (Fig. S5 in the SI), two conformational clusters need to be sampled, which leads to high uncertainties for JNK1. While most of the ML/MM simulations show a preference for the peak on the right side, ligand 18634\_1 mostly samples the left peak. In 18628\_1, the MM simulation shows an unusual extra peak on the left side, which is not present in the other MM simulations. Therefore, the high MAE of JNK1 are the result of sampling errors in the end-state corrections of those two ligands.

The sampling of the MM simulations also influences the variance of the end-state corrections. While the overall MAE of the end-state corrections with OFF2.2.0 exhibits a standard deviation of  $1.1 \text{ kcal mol}^{-1}$ , the corresponding standard deviation of the MAE with refitted torsion potentials from TOR is  $0.8 \text{ kcal mol}^{-1}$ . This difference of  $0.3 \text{ kcal mol}^{-1}$  can be explained by an increased phase space overlap between the MM and ML/MM energy surfaces

in TOR, since both the torsion scans for the refitting and the end-state corrections were conducted with the ANI-2x potential. Therefore, matching the MM and ML/MM energy surfaces with a refitting procedure can also be beneficial for end-state corrections.

## 4 Conclusions

This work represents an independent evaluation of previous reports of improved relative binding free energy results for mechanical embedding ML/MM approaches that treat the intramolecular interactions at the ML level while the protein-ligand interactions and the environment are treated at the MM level. The present ML/MM calculations using mechanical embedding and the ANI-2x potential could reproduce the same level of accuracy as reported in Refs. 52 and 53, with average mean absolute errors of approximately  $0.9 \pm 0.9 \text{ kcal mol}^{-1}$  for the four benchmark systems TYK2, CDK2, JNK1, and P38. This corresponds to what is considered “chemical accuracy”. The underlying MM simulations with OFF 2.2.0 also yield about the same level of accuracy as previously reported for OFF 2.0.0 by Hahn et al.<sup>11</sup> with an MAE of  $0.8 \pm 0.4 \text{ kcal mol}^{-1}$ . Overall, there is no statistically significant difference between the level of accuracy of the mechanical embedding ML/MM and MM RBFE (MAE of 0.9 and  $0.8 \text{ kcal mol}^{-1}$ , respectively). This can be explained by the fact that exactly the same nonbonded parameters were used to calculate the protein-ligand interactions in MM and ML/MM with mechanical embedding. This finding also agrees with a recent report of 589 end-state corrections of hydration free energies with ML/MM using mechanical embedding, where no significant improvements were observed (MAE of  $1.0 \text{ kcal mol}^{-1}$  for both OFF2.0 and ML/MM with mechanical embedding and ANI-2x).<sup>56</sup> Thus, any previously reported performance gains with ML/MM mechanical embedding can probably be attributed to small inadequacies of the intramolecular interactions of the ligand in the employed force fields (OFF 1.0.0 in Ref. 52 and GAFF2.11 in Ref. 53). However, such findings can’t be extrapolated to other force fields or systems.

One potential cause of errors in the intramolecular interactions are the dihedral potentials. In OFF 2.2.0, dihedral potentials are determined with torsion scans of model compounds using DFT with the B3LYP-D3BJ/DZVP level of theory. Here, the Torpenter tool was used to fit the dihedral potentials of all rotatable bonds to ML with ANI-2x. This leads to exactly the same MAE as OFF2.2.0 ( $0.8 \pm 0.4 \text{ kcal mol}^{-1}$ ), which supports the validity of this strategy. Refitting torsions with ML potentials instead of DFT is fast enough to be conducted on the fly, which makes it an interesting option for automated drug discovery pipelines that might explore uncommon regions of chemical space. Compared to end-state corrections with ML/MM, refitting the torsion potentials with ML calculations is computationally less demanding and also does not lead to elevated standard deviations. On average, the standard deviations were  $0.4 \text{ kcal mol}^{-1}$  with MM simulations based on Torpenter, while the corresponding end-state corrections exhibited standard deviations of about  $0.8 \text{ kcal mol}^{-1}$ , which is twice as high. Both options exhibit the same level of accuracy, but the increased precision of Torpenter is likely to lead to a more robust performance, as false positives and negatives due to random fluctuations are avoided. Also, the refitting approach only requires a fraction of the computational costs of ML/MM simulations and does not require significant software changes in the drug discovery pipeline.

While ML/MM simulations with mechanical embedding lead to the same level of accuracy as well-parameterized force fields, they are unlikely to significantly outperform MM simulations because the protein-ligand interactions are still calculated at the MM level. Going forward with ML/MM end-state corrections of protein-ligand binding, there are two main challenges that need to be addressed: First, the low precision of end-state corrections, which arises from the lack of phase space overlap between the MM and ML/MM energy surfaces. This could be addressed with more sampling, enhanced sampling techniques, or the generation of intermediate states between the MM and ML/MM energy surfaces. Using parameter refitting also improved the convergence of the end-state corrections. Second, it will be necessary to increase the accuracy of the ML/MM representation. This could be done by either

employing electrostatic embedding approaches, increasing the size of the ML region, or both. Future work will also explore the use of other ML potentials for protein-ligand binding.

## Supporting Information

Table S1 provides additional error metrics (RMSE,  $R^2$ , and Kendall  $\tau$ ) for the four benchmark systems for the two force fields and the corresponding end-state corrections. Tables S2 to S9 list the RBFE results for each mutation together with the experimental value and the respective end-state corrections. Figures S1 to S8 illustrate the work distributions for the nonequilibrium switching simulations between MM and ML/MM. Figures S9, S10, S11, and S12 show the structures of the ligands used for each benchmark system.

## Acknowledgement

The authors would like to thank Stefan Boresch, Marcus Wieder, and Jody Barbeau for very helpful discussions.

## References

- (1) Williams-Noonan, B. J.; Yuriev, E.; Chalmers, D. K. Free energy methods in drug design: prospects of “alchemical perturbation” in medicinal chemistry: miniperspective. *J. Med. Chem.* **2018**, *61*, 638–649.
- (2) Homeyer, N.; Stoll, F.; Hillisch, A.; Gohlke, H. Binding free energy calculations for lead optimization: assessment of their accuracy in an industrial drug design context. *J. Chem. Theory Comput.* **2014**, *10*, 3331–3344.
- (3) Cournia, Z.; Allen, B.; Sherman, W. Relative binding free energy calculations in drug discovery: recent advances and practical considerations. *J. Chem. Inf. Model.* **2017**, *57*, 2911–2937.
- (4) Muegge, I.; Hu, Y. Recent advances in alchemical binding free energy calculations for drug discovery. *ACS Med. Chem. Lett.* **2023**, *14*, 244–250.
- (5) Karwounopoulos, J.; Wieder, M.; Boresch, S. Relative binding free energy calculations with transformato: A molecular dynamics engine-independent tool. *Front. Mol. Biosci.* **2022**, *9*, 850.



- (6) Shirts, M. R.; Mobley, D. L.; Brown, S. P. Free-energy calculations in structure-based drug design. *Drug Design* **2010**, *1*, 61–86.
- (7) Mobley, D. L.; Klimovich, P. V. Perspective: Alchemical free energy calculations for drug discovery. *J. Chem. Phys.* **2012**, *137*.
- (8) König, G.; Sokkar, P.; Pryk, N.; Heinrich, S.; Moeller, D.; Camicata, G.; Matzov, D.; Dietze, P.; Thiel, W.; Bashan, A.; Bandow, J. E.; Zuegg, J.; Yonath, A.; Schulz, F.; Sanchez-Garcia, E. Rational prioritization strategy allows the design of macrolide derivatives that overcome antibiotic resistance. *Proc. Natl. Acad. Sci. USA* **2021**, *118*, e2113632118.
- (9) Xue, B.; Yang, Q.; Zhang, Q.; Wan, X.; Fang, D.; Lin, X.; Sun, G.; Gobbo, G.; Cao, F.; Mathiowetz, A. M.; others Development and comprehensive benchmark of a high-quality amber-consistent small molecule force field with broad chemical space coverage for molecular modeling and free energy calculation. *Journal of Chemical Theory and Computation* **2023**, *20*, 799–818.
- (10) Burger, P. B.; Hu, X.; Balabin, I.; Muller, M.; Stanley, M.; Joubert, F.; Kaiser, T. M. FEP Augmentation as a Means to Solve Data Paucity Problems for Machine Learning in Chemical Biology. *J. Chem. Inf. Model.* **2024**, *64*, 3812–3825.
- (11) Hahn, D. F.; Gapsys, V.; de Groot, B. L.; Mobley, D. L.; Tresadern, G. Current State of Open Source Force Fields in Protein–Ligand Binding Affinity Predictions. *J. Chem. Inf. Model.* **2024**, *64*(13), 5063—5076.
- (12) Lee, T.-S.; Allen, B. K.; Giese, T. J.; Guo, Z.; Li, P.; Lin, C.; McGee Jr, T. D.; Pearlman, D. A.; Radak, B. K.; Tao, Y.; Tsai, H.-C.; Xu, H.; Sherman, W.; York, D. M. Alchemical binding free energy calculations in AMBER20: Advances and best practices for drug discovery. *J. Chem. Inf. Model.* **2020**, *60*, 5595–5623.
- (13) Schindler, C. E.; Baumann, H.; Blum, A.; Böse, D.; Buchstaller, H.-P.; Burgdorf, L.; Cappel, D.; Chekler, E.; Czodrowski, P.; Dorsch, D.; Eguida, M.; Follows, B.; Fuchß, T.; Grädler, U.; Gunera, J.; Johnson, T.; Jorand, C.; Karra, S.; Klein, M.; Knehans, T.; Koetzner, L.; Krier, M.; Leiendecker, M.; Leuthner, B.; Li, L.; Mochalkin, I.; Musil, D.; Neagu, C.; Rippmann, F.; Schiemann, K.; Schulz, R.; Steinbrecher, T.; Tanzer, E.-M.; Unzue Lopez, A.; Viacava Follis, A.; Wegener, A.; Kuhn, D. Large-scale assessment of binding free energy calculations in active drug discovery projects. *J. Chem. Inf. Model.* **2020**, *60*, 5457–5474.
- (14) van Gunsteren, W. F.; Daura, X.; Hansen, N.; Mark, A. E.; Oostenbrink, C.; Riniker, S.; Smith, L. J. Validation of molecular simulation: an overview of issues. *Angew. Chem. Int. Ed.* **2018**, *57*, 884–902.
- (15) Gao, J.; Xia, X. A priori evaluation of aqueous polarization effects through Monte Carlo QM-MM simulations. *Science* **1992**, *258*, 631–5.

- (16) Gao, J.; Luque, F. J.; Orozco, M. Induced dipole moment and atomic charges based on average electrostatic potentials in aqueous solution. *J. Chem. Phys.* **1993**, *98*, 2975.
- (17) Luzhkov, V.; Warshel, A. Microscopic models for quantum mechanical calculations of chemical processes in solutions: LD/AMPAC and SCAAS/AMPAC calculations of solvation energies. *J. Comput. Chem.* **1992**, *13*, 199–213.
- (18) Wesolowski, T.; Warshel, A. Ab Initio Free Energy Perturbation Calculations of Solvation Free Energy Using the Frozen Density Functional Approach. *J. Phys. Chem.* **1994**, *98*, 5183–5187.
- (19) Gao, J.; Freindorf, M. Hybrid ab Initio QM/MM Simulation of N -Methylacetamide in Aqueous Solution. *J. Phys. Chem. A* **1997**, *101*, 3182–3188.
- (20) Reddy, M. R.; Singh, U. C.; Erion, M. D. Use of a QM/MM-based FEP method to evaluate the anomalous hydration behavior of simple alkyl amines and amides: Application to the design of FBPase inhibitors for the treatment of type-2 diabetes. *J. Am. Chem. Soc.* **2011**, *133*, 8059–8061.
- (21) Cui, Q.; Elstner, M. “Multi-Scale” QM/MM Methods with Self-Consistent-Charge Density-Functional-Tight-Binding (SCC-DFTB). *Chall. Adv. Comput. Che.* **2009**, *7*, 173–196.
- (22) König, G.; Hudson, P. S.; Boresch, S.; Woodcock, H. L. Multiscale Free Energy Simulations: An Efficient Method for Connecting Classical MD Simulations to QM or QM/MM Free Energies Using Non-Boltzmann Bennett Reweighting Schemes. *J. Chem. Theory Comput.* **2014**, *10*, 1406–1419.
- (23) Valiev, M.; Bylaska, E. J.; Dupuis, M.; Tratnyek, P. G. Combined Quantum Mechanical and Molecular Mechanics Studies of the Electron-Transfer Reactions Involving Carbon Tetrachloride in Solution. *J. Phys. Chem. A* **2008**, *112*, 2713–2720.
- (24) Zheng, L.; Chen, M.; Yang, W. Random walk in orthogonal space to achieve efficient free-energy simulation of complex systems. *Proc. Natl. Acad. Sci. U.S.A.* **2008**, *105*, 20227–32.
- (25) Beierlein, F. R.; Michel, J.; Essex, J. W. A Simple QM/MM Approach for Capturing Polarization Effects in Protein-Ligand Binding Free Energy Calculations. *J. Phys. Chem. B* **2011**, *115*, 4911–4926.
- (26) Heimdal, J.; Ryde, U. Convergence of QM/MM free-energy perturbations based on molecular-mechanics or semiempirical simulations. *Phys. Chem. Chem. Phys* **2012**, *14*, 12592–12604.
- (27) Fox, S. J.; Pittock, C.; Tautermann, C. S.; Fox, T.; Christ, C.; Malcolm, N. O. J.; Essex, J. W.; Skylaris, C.-K. Free energies of binding from large-scale first-principles quantum mechanical calculations: application to ligand hydration energies. *J. Phys. Chem. B* **2013**, *117*, 9478–9485.

- (28) König, G.; Pickard, F. C.; Mei, Y.; Brooks, B. R. Predicting hydration free energies with a hybrid QM/MM approach: an evaluation of implicit and explicit solvation models in SAMPL4. *J. Comput.-Aid. Mol. Design* **2014**, *28*, 245–257.
- (29) Sampson, C.; Fox, T.; Tautermann, C. S.; Woods, C.; Skylaris, C.-K. A “Stepping Stone” Approach for Obtaining Quantum Free Energies of Hydration. *J. Phys. Chem. B* **2015**, *119*, 7030–7040.
- (30) Cave-Ayland, C.; Skylaris, C.-K.; Essex, J. W. Direct Validation of the Single Step Classical to Quantum Free Energy Perturbation. *J. Phys. Chem. B* **2015**, *119*, 1017–1025.
- (31) König, G.; Mei, Y.; Pickard, F. C.; Simmonett, A. C.; Miller, B. T.; Herbert, J. M.; Woodcock, H. L.; Brooks, B. R.; Shao, Y. Computation of Hydration Free Energies Using the Multiple Environment Single System Quantum Mechanical/Molecular Mechanical Method. *J. Chem. Theory Comput.* **2016**, *12*, 332–344.
- (32) Pickard, F. C.; König, G.; Tofoleanu, F.; Lee, J.; Simmonett, A. C.; Shao, Y.; Ponder, J. W.; Brooks, B. R. Blind prediction of distribution in the SAMPL5 challenge with QM based protomer and  $pK_a$  corrections. *J. Comput.-Aided Mol. Des.* **2016**, *30*, 1087–1100.
- (33) Giese, T. J.; York, D. M. Development of a Robust Indirect Approach for MM  $\rightarrow$  QM Free Energy Calculations That Combines Force-Matched Reference Potential and Bennett’s Acceptance Ratio Methods. *Journal of chemical theory and computation* **2019**, *15*, 5543–5562.
- (34) König, G.; Pickard, F. C.; Huang, J.; Simmonett, A. C.; Tofoleanu, F.; Lee, J.; Dral, P. O.; Prasad, S.; Jones, M.; Shao, Y.; Thiel, W.; Brooks, B. R. Calculating distribution coefficients based on multi-scale free energy simulations: an evaluation of MM and QM/MM explicit solvent simulations of water-cyclohexane transfer in the SAMPL5 challenge. *J. Comput.-Aided Mol. Des.* **2016**, *30*, 989–1006.
- (35) Cui, Q.; Pal, T.; Xie, L. Biomolecular QM/MM Simulations: What Are Some of the “Burning Issues”? *J. Phys. Chem. B* **2021**, *125*, 689–702.
- (36) Pickard, F. C.; König, G.; Simmonett, A. C.; Shao, Y.; Brooks, B. R. An efficient protocol for obtaining accurate hydration free energies using quantum chemistry and reweighting from molecular dynamics simulations. *Biorg. Med. Chem.* **2016**, *24*, 4988–4997.
- (37) König, G.; Brooks, B. R.; Thiel, W.; York, D. M. On the convergence of multi-scale free energy simulations. *Mol. Simulat.* **2018**, *44*, 1062–1081.
- (38) König, G.; Pickard, F.; Huang, J.; Thiel, W.; MacKerell, A.; Brooks, B.; York, D. A Comparison of QM/MM Simulations with and without the Drude Oscillator Model Based on Hydration Free Energies of Simple Solutes. *Molecules* **2018**, *23*, 2695.

- (39) Giese, T. J.; York, D. M. Development of a Robust Indirect Approach for MM→ QM Free Energy Calculations that Combines Force-matched Reference Potential and Bennett’s Acceptance Ratio Methods. *J. Chem. Theory Comput.* **2019**, *15*, 5543–5562.
- (40) König, G.; Riniker, S. On the faithfulness of molecular mechanics representations of proteins towards quantum-mechanical energy surfaces. *Interface Focus* **2020**, *10*, 20190121.
- (41) Hudson, P. S.; Boresch, S.; Rogers, D. M.; Woodcock, H. L. Accelerating QM/MM free energy computations via intramolecular force matching. *J. Chem. Theory Comput.* **2018**, *14*, 6327–6335.
- (42) Horton, J. T.; Boothroyd, S.; Wagner, J.; Mitchell, J. A.; Gokey, T.; Dotson, D. L.; Behara, P. K.; Ramaswamy, V. K.; Mackey, M.; Chodera, J. D.; Anwar, J.; Mobley, D. L.; Cole, D. J. Open force field BespokeFit: automating bespoke torsion parametrization at scale. *J. Chem. Inf. Model.* **2022**, *62*, 5622–5633.
- (43) Kearns, F. L.; Hudson, P. S.; Woodcock, H. L.; Boresch, S. Computing converged free energy differences between levels of theory via nonequilibrium work methods: Challenges and opportunities. *J. Comput. Chem.* **2017**, *38*, 1376–1388.
- (44) Hudson, P. S.; Woodcock, H. L.; Boresch, S. Use of Nonequilibrium Work Methods to Compute Free Energy Differences Between Molecular Mechanical and Quantum Mechanical Representations of Molecular Systems. *J. Phys. Chem. Lett.* **2015**, *6*, 4850–4856.
- (45) Kulichenko, M.; Smith, J. S.; Nebgen, B.; Li, Y. W.; Fedik, N.; Boldyrev, A. I.; Lubbers, N.; Barros, K.; Tretiak, S. The Rise of Neural Networks for Materials and Chemical Dynamics. *J. Phys. Chem. Lett.* **2021**, *12*, 6227–6243.
- (46) Dral, P. O. Quantum chemistry in the age of machine learning. *J. Phys. Chem. Lett.* **2020**, *11*, 2336–2347.
- (47) Smith, J. S.; Isayev, O.; Roitberg, A. E. ANI-1: an extensible neural network potential with DFT accuracy at force field computational cost. *Chem. Sci.* **2017**, *8*, 3192–3203.
- (48) Smith, J. S.; Nebgen, B. T.; Zubatyuk, R.; Lubbers, N.; Devereux, C.; Barros, K.; Tretiak, S.; Isayev, O.; Roitberg, A. E. Approaching coupled cluster accuracy with a general-purpose neural network potential through transfer learning. *Nat. Commun.* **2019**, *10*, 2903.
- (49) Devereux, C.; Smith, J. S.; Huddleston, K. K.; Barros, K.; Zubatyuk, R.; Isayev, O.; Roitberg, A. E. Extending the applicability of the ANI deep learning molecular potential to sulfur and halogens. *J. Chem. Theory Comput.* **2020**, *16*, 4192–4202.
- (50) Park, S.; Han, H.; Kim, H.; Choi, S. Machine Learning Applications for Chemical Reactions. *Chem. Asian J.* **2022**, *17*, e202200203.

- (51) Han, F.; Hao, D.; He, X.; Wang, L.; Niu, T.; Wang, J. Distribution of Bound Conformations in Conformational Ensembles for X-ray Ligands Predicted by the ANI-2X Machine Learning Potential. *J. Chem. Inf. Model.* **2023**, *63*, 6608–6618.
- (52) Rufa, D. A.; Bruce Macdonald, H. E.; Fass, J.; Wieder, M.; Grinaway, P. B.; Roitberg, A. E.; Isayev, O.; Chodera, J. D. Towards chemical accuracy for alchemical free energy calculations with hybrid physics-based machine learning/molecular mechanics potentials. *BioRxiv* **2020**, 2020–07.
- (53) Sabanés Zariquiey, F.; Galvelis, R.; Gallicchio, E.; Chodera, J. D.; Markland, T. E.; De Fabritiis, G. Enhancing Protein–Ligand Binding Affinity Predictions Using Neural Network Potentials. *J. Chem. Inf. Model.* **2024**, *64*, 1481–1485.
- (54) Akkus, E.; Tayfuroglu, O.; Yildiz, M.; Kocak, A. Accurate Binding Free Energy Method from End-State MD Simulations. *J. Chem. Inf. Model.* **2022**, *62*, 4095–4106.
- (55) Tkaczyk, S.; Karwounopoulos, J.; Schöller, A.; Woodcock, H. L.; Langer, T.; Boresch, S.; Wieder, M. Reweighting from Molecular Mechanics Force Fields to the ANI-2x Neural Network Potential. *J. Chem. Theory Comput.* **2024**, *20*, 2719–2728.
- (56) Karwounopoulos, J.; Wu, Z.; Tkaczyk, S.; Wang, S.; Baskerville, A.; Ranasinghe, K.; Langer, T.; Wood, G. P.; Wieder, M.; Boresch, S. Insights and Challenges in Correcting Force Field Based Solvation Free Energies Using A Neural Network Potential. *J. Phys. Chem. B* **2024**, *128*, 6693–6703.
- (57) Horton, J. T.; Allen, A. E.; Dodda, L. S.; Cole, D. J. QUBEKit: Automating the derivation of force field parameters from quantum mechanics. *J. Chem. Inf. Model.* **2019**, *59*, 1366–1381.
- (58) Morado, J.; Mortenson, P. N.; Nissink, J. W. M.; Essex, J. W.; Skylaris, C.-K. Does a machine-learned potential perform better than an optimally tuned traditional force field? a case study on fluorohydrins. *J. Chem. Inf. Model.* **2023**, *63*, 2810–2827.
- (59) Lahey, S.-L. J.; Thien Phuc, T. N.; Rowley, C. N. Benchmarking force field and the ANI neural network potentials for the torsional potential energy surface of biaryl drug fragments. *J. Chem. Inf. Model.* **2020**, *60*, 6258–6268.
- (60) Liang, J.; Tsui, V.; Van Abbema, A.; Bao, L.; Barrett, K.; Beresini, M.; Berezhkovskiy, L.; Blair, W. S.; Chang, C.; Driscoll, J.; Eigenbrot, C.; Ghilardi, N.; Gibbons, P.; Halladay, J.; Johnson, A.; Kohli, P. B.; Lai, Y.; Liimatta, M.; Mantik, P.; Menghrajani, K.; Murray, J.; Sambrone, A.; Xiao, Y.; Shia, S.; Shin, Y.; Smith, J.; Sohn, S.; Stanley, M.; Ultsch, M.; Zhang, B.; Wu, L. C.; Magnuson, S. Lead identification of novel and selective TYK2 inhibitors. *Eur. J. Med. Chem.* **2013**, *67*, 175–187.
- (61) Liang, J.; van Abbema, A.; Balazs, M.; Barrett, K.; Berezhkovsky, L.; Blair, W.; Chang, C.; Delarosa, D.; DeVoss, J.; Driscoll, J.; Eigenbrot, C.; Ghilardi, N.; Gibbons, P.; Halladay, J.; Johnson, A.; Kohli, P. B.; Lai, Y.; Liu, Y.; Lyssikatos, J.; Mantik, P.; Menghrajani, K.; Murray, J.; Sambrone, A.; Shia, S.; Shin, Y.; Smith, J.;

- Sohn, S.; Tsui, V.; Ultsch, M.; Wu, L. C.; Xiao, Y.; Young, J.; Zhang, B.; Zhu, B.; Magnuson, S. Lead optimization of a 4-aminopyridine benzamide scaffold to identify potent, selective, and orally bioavailable TYK2 inhibitors. *J. Med. Chem.* **2013**, *56*, 4521–4536.
- (62) Hardcastle, I. R.; Arris, C. E.; Bentley, J.; Boyle, F. T.; Chen, Y.; Curtin, N. J.; Endicott, J. A.; Gibson, A. E.; Golding, B. T.; Griffin, R. J.; Jewsbury, P.; Menyerol, J.; Mesguiche, V.; Newell, D. R.; Noble, M. E. M.; Pratt, D. J.; Wang, L.-Z.; Whitfield, H. J. N2-substituted O 6-cyclohexylmethylguanidine derivatives: potent inhibitors of cyclin-dependent kinases 1 and 2. *J. Med. Chem.* **2004**, *47*, 3710–3722.
- (63) Szczepankiewicz, B. G.; Kosogof, C.; Nelson, L. T.; Liu, G.; Liu, B.; Zhao, H.; Serby, M. D.; Xin, Z.; Liu, M.; Gum, R. J.; Haasch, D. L.; Wang, S.; Clampit, J. E.; Johnson, E. F.; Lubben, T. H.; Stashko, M. A.; Olejniczak, E. T.; Sun, C.; Dorwin, S. A.; Haskins, K.; Abad-Zapatero, C.; Fry, E. H.; Hutchins, C. W.; Sham, H. L.; Rondinone, C. M.; Trevillyan, J. M. Aminopyridine-based c-Jun N-terminal kinase inhibitors with cellular activity and minimal cross-kinase activity. *J. Med. Chem.* **2006**, *49*, 3563–3580.
- (64) Goldstein, D. M.; Soth, M.; Gabriel, T.; Dewdney, N.; Kuglstatler, A.; Arzeno, H.; Chen, J.; Bingenheimer, W.; Dalrymple, S. A.; Dunn, J.; Farrell, R.; Frauchiger, S.; La Fargue, J.; Ghate, M.; Graves, B.; Hill, R. J.; Li, F.; Litman, R.; Loe, B.; McIntosh, J.; McWeeney, D.; Papp, E.; Park, J.; Reese, H. F.; Roberts, R. T.; Rotstein, D.; San Pablo, B.; Sarma, K.; Stahl, M.; Sung, M.-L.; Suttman, R. T.; Sjogren, E. B.; Tan, Y.; Trejo, A.; Welch, M.; Weller, P.; Wong, B. R.; Zecic, H. Discovery of 6-(2, 4-Difluorophenoxy)-2-[3-hydroxy-1-(2-hydroxyethyl) propylamino]-8-methyl-8 H-pyrido [2, 3-d] pyrimidin-7-one (Pamapimod) and 6-(2, 4-Difluorophenoxy)-8-methyl-2-(tetrahydro-2 H-pyran-4-ylamino) pyrido [2, 3-d] pyrimidin-7 (8 H)-one (R1487) as Orally Bioavailable and Highly Selective Inhibitors of p38 $\alpha$  Mitogen-Activated Protein Kinase. *J. Med. Chem.* **2011**, *54*, 2255–2265.
- (65) Wang, L.; Wu, Y.; Deng, Y.; Kim, B.; Pierce, L.; Krilov, G.; Lupyan, D.; Robinson, S.; Dahlgren, M. K.; Greenwood, J.; Romero, D. L.; Masse, C.; Knight, J. L.; Steinbrecher, T.; Beuming, T.; Damm, W.; Harder, E.; Sherman, W.; Brewer, M.; Wester, R.; Murcko, M.; Frye, L.; Farid, R.; Lin, T.; Mobley, D. L.; Jorgensen, W. L.; Berne, B. J.; Friesner, R. A.; Abel, R. Accurate and reliable prediction of relative ligand binding potency in prospective drug discovery by way of a modern free-energy calculation protocol and force field. *J. Am. Chem. Soc.* **2015**, *137*, 2695–2703.
- (66) Tembe, B. L.; McCammon, J. A. Ligand-receptor interactions. *Comput. Chem.* **1984**, *8*, 281–283.
- (67) *Manuscript in preparation.*
- (68) Liu, S.; Wu, Y.; Lin, T.; Abel, R.; Redmann, J. P.; Summa, C. M.; Jaber, V. R.; Lim, N. M.; Mobley, D. L. Lead optimization mapper: automating free energy calculations for lead optimization. *J. Comput.-Aided Mol. Des.* **2013**, *27*, 755–770.

- (69) Fleck, M.; Wieder, M.; Boresch, S. Dummy atoms in alchemical free energy calculations. *J. Chem. Theory Comput.* **2021**, *17*, 4403–4419.
- (70) Roe, D. R.; Brooks, B. R. A protocol for preparing explicitly solvated systems for stable molecular dynamics simulations. *J. Chem. Phys.* **2020**, *153*.
- (71) Åqvist, J.; Wennerström, P.; Nervall, M.; Bjelic, S.; Brandsdal, B. O. Molecular dynamics simulations of water and biomolecules with a Monte Carlo constant pressure algorithm. *Chem. Phys. Lett.* **2004**, *384*, 288–294.
- (72) Sugita, Y.; Okamoto, Y. Replica-exchange molecular dynamics method for protein folding. *Chem. Phys. Lett.* **1999**, *314*, 141–151.
- (73) Swendsen, R. H.; Wang, J. S. Replica monte-carlo simulation of spin glasses. *Phys. Rev. Lett.* **1986**, *57*, 2607.
- (74) Giese, T. J.; York, D. M. Variational method for networkwide analysis of relative ligand binding free energies with loop closure and experimental constraints. *J. Chem. Theory Comput.* **2021**, *17*, 1326–1336.
- (75) Qiu, Y.; Smith, D. G.; Stern, C. D.; Feng, M.; Jang, H.; Wang, L.-P. Driving torsion scans with wavefront propagation. *J. Chem. Phys.* **2020**, *152*.
- (76) Larsen, A. H.; Mortensen, J. J.; Blomqvist, J.; Castelli, I. E.; Christensen, R.; Dulak, M.; Friis, J.; Groves, M. N.; Hammer, B.; Hargus, C.; Hermes, E. D.; Jennings, P. C.; Jensen, P. B.; Kermode, J.; Kitchin, J. R.; Kolsbjerg, E. L.; Kubal, J.; Kaasbjerg, K.; Lysgaard, S.; Maronsson, J. B.; Maxson, T.; Olsen, T.; Pastewka, L.; Peterson, A.; Rostgaard, C.; Schiøtz, J.; Schütt, O.; Strange, M.; Thygesen, K. S.; Vegge, T.; Vilhelmsen, L.; Walter, M.; Zeng, Z.; Jacobsen, K. W. The atomic simulation environment—a Python library for working with atoms. *J. Phys. Condens. Matter.* **2017**, *29*, 273002.
- (77) Eastman, P.; Galvelis, R.; Peláez, R. P.; Abreu, C. R. A.; Farr, S. E.; Gallicchio, E.; Gorenko, A.; Henry, M. M.; Hu, F.; Huang, J.; Krämer, A.; Michel, J.; Mitchell, J. A.; Pande, V. S.; Rodrigues, J. P.; Rodriguez-Guerra, J.; Simmonett, A. C.; Singh, S.; Swails, J.; Turner, P.; Wang, Y.; Zhang, I.; Chodera, J. D.; De Fabritiis, G.; Markland, T. E. OpenMM 8: Molecular Dynamics Simulation with Machine Learning Potentials. *The Journal of Physical Chemistry B* **2023**, *128*, 109–116.
- (78) Wang, L.-P.; Chen, J.; Van Voorhis, T. Systematic parametrization of polarizable force fields from quantum chemistry data. *J. Chem. Theory Comput.* **2013**, *9*, 452–460.
- (79) Qiu, Y.; Smith, D. G.; Boothroyd, S.; Jang, H.; Hahn, D. F.; Wagner, J.; Bannan, C. C.; Gokey, T.; Lim, V. T.; Stern, C. D.; others Development and benchmarking of open force field v1.0.0—the parsley small-molecule force field. *J. Chem. Theory Comput.* **2021**, *17*, 6262–6280.
- (80) Crooks, G. E. Path-ensemble averages in systems driven far from equilibrium. *Phys. Rev. E* **2000**, *61*, 2361–2366.

- (81) Boothroyd, S.; Behara, P. K.; Madin, O. C.; Hahn, D. F.; Jang, H.; Gapsys, V.; Wagner, J. R.; Horton, J. T.; Dotson, D. L.; Thompson, M. W.; others Development and benchmarking of open force field 2.0.0: the Sage small molecule force field. *J. Chem. Theory Comput.* **2023**, *19*, 3251–3275.
- (82) Jorgensen, W. L.; Chandrasekhar, J.; Madura, J. D. Comparison of simple potential functions for simulating liquid water. *J. Chem. Phys.* **1983**, *79*, 926–935.
- (83) Miyamoto, S.; Kollman, P. A. Settle: An analytical version of the SHAKE and RATTLE algorithm for rigid water models. *J. Comput. Chem.* **1992**, *13*, 952–962.
- (84) Åqvist, J.; Wennerström, P.; Nervall, M.; Bjelic, S.; Brandsdal, B. O. Molecular dynamics simulations of water and biomolecules with a Monte Carlo constant pressure algorithm. *Chem. Phys. Lett.* **2004**, *384*, 288–294.
- (85) Chow, K. H.; Ferguson, D. M. Isothermal-isobaric molecular dynamics simulations with Monte Carlo volume sampling. *Comput. Phys. Commun.* **1995**, *91*, 283–289.
- (86) Darden, T.; York, D.; Pedersen, L. Particle Mesh Ewald - An N.Log(N) method for Ewald sums in large systems. *J. Chem. Phys.* **1993**, *98*, 10089–10092.
- (87) Essmann, U.; Perera, L.; Berkowitz, M. L.; Darden, T.; Lee, H.; Pedersen, L. G. A smooth particle mesh Ewald method. *J. Chem. Phys.* **1995**, *103*, 8577.
- (88) Galvelis, R.; Varela-Rial, A.; Doerr, S.; Fino, R.; Eastman, P.; Markland, T. E.; Chodera, J. D.; De Fabritiis, G. NNP/MM: Accelerating Molecular Dynamics Simulations with Machine Learning Potentials and Molecular Mechanics. *J. Chem. Inf. Model* **2023**, *63*, 5701–5708.
- (89) Shirts, M. R.; Chodera, J. D. Statistically optimal analysis of samples from multiple equilibrium states. *J. Chem. Phys.* **2008**, *129*, 124105.
- (90) Dellago, C.; Hummer, G. Computing equilibrium free energies using non-equilibrium molecular dynamics. *Entropy* **2013**, *16*, 41–61.
- (91) Wang, M.; Mei, Y.; Ryde, U. Predicting relative binding affinity using nonequilibrium QM/MM simulations. *J. Chem. Theory Comput.* **2018**, *14*, 6613–6622.
- (92) Kearns, F. L.; Warrensford, L.; Boresch, S.; Woodcock, H. L. The Good, the Bad, and the Ugly: “HiPen”, a New Dataset for Validating (S) QM/MM Free Energy Simulations. *Molecules* **2019**, *24*, 681.
- (93) Wu, J. Z.; Azimi, S.; Khuttan, S.; Deng, N.; Gallicchio, E. Alchemical transfer approach to absolute binding free energy estimation. *J. Chem. Theory Comput.* **2021**, *17*, 3309–3319.



# Supplementary Information: An evaluation of machine learning/molecular mechanics end-state corrections with mechanical embedding to calculate relative protein-ligand binding free energies

Johannes Karwounopoulos,<sup>†,‡</sup> Mateusz Bieniek,<sup>†,‡</sup> Zhiyi Wu,<sup>†</sup> Adam Baskerville,<sup>†</sup>  
Gerhard König,<sup>\*,†</sup> Benjamin P. Cossins,<sup>†</sup> and Geoffrey P. F. Wood<sup>†</sup>

<sup>†</sup>*Exscientia, Schrödinger Building, Oxford Science Park, Oxford, UK*

<sup>‡</sup>*Contributed equally*

E-mail: gkoenig@exscientia.co.uk

Table S1: Comparison of the root mean square errors (RMSE), correlations coefficients ( $R^2$ ), Kendall  $\tau$  of the relative binding free energies using the OpenFF force field 2.2.0 (OFF2.2.0), the refitted force field based on torsion potentials from Torpenter with ANI-2x (TOR), and the corresponding end-state corrected metrics (EC) using ANI-2x. The last row shows the average results over all 108 relative binding free energies. All RMSE are in kcal mol<sup>-1</sup>.

	MM						ML/MM					
	OFF2.2.0			TOR			EC-OFF2.2.0			EC-TOR		
	RMSE	$R^2$	$\tau$	RMSE	$R^2$	$\tau$	RMSE	$R^2$	$\tau$	RMSE	$R^2$	$\tau$
TYK2	0.8	0.6	0.5	1.0	0.6	0.5	0.9	0.7	0.5	0.7	0.7	0.5
CDK2	0.9	0.6	0.5	0.8	0.6	0.6	0.7	0.7	0.6	1.0	0.5	0.4
JNK1	0.7	0.3	0.4	0.7	0.4	0.5	1.5	0.1	-0.1	1.1	0.0	0.1
P38	1.2	0.5	0.5	1.3	0.5	0.5	1.2	0.5	0.5	1.3	0.4	0.5
<b>Average</b>	<b>1.0</b>	<b>0.5</b>	<b>0.5</b>	<b>1.1</b>	<b>0.5</b>	<b>0.5</b>	<b>1.1</b>	<b>0.4</b>	<b>0.5</b>	<b>1.1</b>	<b>0.4</b>	<b>0.4</b>

Table S2: TYK2 relative binding free energy results, based on MM simulations with Open Force Field (OFF2.2.0), reparameterized torsion potentials with Torpenter (TOR) and end-state corrections (EC) based on mechanical embedding with ANI-2x. The error bars show the respective standard deviations. The experimental reference results are denoted with EXP. All data are in kcal mol<sup>-1</sup>.

Ligand A	Ligand B	EXP	OFF2.2.0	EC-OFF2.2.0	TOR	EC-TOR
ejm_31	ejm_45	0	0.1 ± 0.2	-0.7 ± 1.1	-0.5 ± 0.2	0.4 ± 0.9
ejm_31	ejm_47	-0.2	0.2 ± 0.5	-0.6 ± 1.1	-0.8 ± 0.2	-0.4 ± 1.0
ejm_31	ejm_48	0.5	0.8 ± 0.4	-0.1 ± 1.2	-0.3 ± 0.4	-0.3 ± 1.1
ejm_31	ejm_49	1.8	0.2 ± 0.1	-0.4 ± 1.2	-1.1 ± 0.2	0.7 ± 0.9
ejm_31	jmc_23	-2.2	-1.5 ± 0.3	-2.9 ± 1.2	-3.4 ± 0.3	-2.7 ± 1.1
ejm_31	jmc_27	-1.7	-1.6 ± 0.1	-3.3 ± 1.1	-3.3 ± 0.4	-3.1 ± 1.1
ejm_42	ejm_43	1.5	1.6 ± 0.2	1.6 ± 0.8	1.4 ± 0.1	1.6 ± 0.6
ejm_42	ejm_50	0.8	0.2 ± 0.1	0.4 ± 0.7	0.6 ± 0.1	1.2 ± 0.6
ejm_42	ejm_54	-0.8	-0.2 ± 0.4	-0.4 ± 0.8	-0.3 ± 0.2	-0.6 ± 0.5
ejm_43	ejm_44	0.8	1.4 ± 0.2	0.9 ± 0.7	1.1 ± 0.1	0.6 ± 0.5
ejm_44	ejm_55	-1.8	-2.9 ± 0.2	-2 ± 0.8	-1.8 ± 0.2	-2.7 ± 0.4
ejm_45	ejm_50	0.6	0.1 ± 0.3	0.1 ± 0.8	0.4 ± 0.2	0.6 ± 0.4
ejm_46	jmc_27	0	-0.5 ± 0.1	-0.2 ± 0.6	-1.0 ± 0.1	-1.1 ± 0.7
ejm_46	jmc_30	0.4	-0.7 ± 0.1	0.4 ± 0.7	-0.8 ± 0.2	0.2 ± 0.6
ejm_47	ejm_55	0.5	-0.2 ± 0.3	0 ± 0.8	0.7 ± 0.1	-0.4 ± 0.5
ejm_48	ejm_49	1.3	-0.6 ± 0.4	-0.3 ± 1.1	-0.8 ± 0.4	1.0 ± 0.8
ejm_54	ejm_55	1.3	0.3 ± 0.1	1.0 ± 0.8	1.0 ± 0.1	0.2 ± 0.1
jmc_23	jmc_28	0.7	0.6 ± 0.1	0.3 ± 0.8	0.8 ± 0.1	1.0 ± 0.6
jmc_27	jmc_28	0.3	0.8 ± 0.1	0.8 ± 0.7	0.7 ± 0.0	1.4 ± 0.5
jmc_27	jmc_30	0.3	-0.2 ± 0.1	0.5 ± 0.8	0.2 ± 0.1	1.3 ± 0.5

Table S3: CDK2 relative binding free energy results, based on MM simulations with Open Force Field (OFF2.2.0), reparameterized torsion potentials with Torpenter (TOR) and end-state corrections (EC) based on mechanical embedding with ANI-2x. The error bars show the respective standard deviations. The experimental reference results are denoted with EXP. All data are in kcal mol<sup>-1</sup>.

Ligand A	Ligand B	EXP	OFF2.2.0	EC-OFF2.2.0	TOR	EC-TOR
1h1q	1h1r	0.51	-0.9 ± 0.1	-0.1 ± 0.6	-0.9 ± 0.1	-0.1 ± 0.2
1h1q	1oi9	-1.56	-2.1 ± 0.3	-1.7 ± 0.6	-1.9 ± 0.6	-1.9 ± 0.7
1h1r	1oiu	-1.42	-1.4 ± 0.6	-0.3 ± 0.9	-1.4 ± 0.3	-0.2 ± 0.8
1h1r	20	-1.03	-0.4 ± 0.1	-1.0 ± 0.6	-0.4 ± 0.1	-0.3 ± 0.4
1h1r	21	-0.14	0.3 ± 0.1	-0.1 ± 0.2	0.3 ± 0.1	-0.3 ± 0.3
1h1r	22	-0.18	0 ± 0.3	0.5 ± 0.4	-0.1 ± 0.1	-0.4 ± 0.2
1h1s	28	0.15	0.5 ± 0.2	0.7 ± 0.7	0.6 ± 0.5	0.4 ± 0.7
1h1s	29	1.38	0.6 ± 0.4	1.5 ± 0.8	1.1 ± 0.6	1.6 ± 0.8
1h1s	30	1.45	1.5 ± 0.1	2.5 ± 0.7	1.1 ± 0.1	1.9 ± 0.4
1h1s	32	1.51	-0.7 ± 0.3	0.6 ± 0.8	0.5 ± 0.1	-0.4 ± 0.5
1oi9	26	1.32	-0.1 ± 0.3	-0.1 ± 0.3	0.1 ± 0.5	0.2 ± 0.7
1oiu	22	1.24	1.3 ± 0.6	0.7 ± 0.9	1.3 ± 0.2	-0.2 ± 0.7
1oiy	26	1.37	0.7 ± 1	1.3 ± 1	-0.3 ± 0.4	-0.5 ± 0.5
1oiy	31	0.27	0.5 ± 1	1.1 ± 1	1.0 ± 1.2	0.8 ± 1.2
21	32	-1.93	-3.4 ± 0.3	-2.8 ± 0.3	-2.1 ± 0.5	-3.4 ± 0.7
28	30	1.3	1.0 ± 0.3	1.9 ± 0.3	0.5 ± 0.4	1.4 ± 0.6
29	31	0.35	0.4 ± 0.6	0.2 ± 0.6	1.1 ± 0.1	0.8 ± 0.4

Table S4: JNK1 relative binding free energy results, based on MM simulations with Open Force Field (OFF2.2.0), reparameterized torsion potentials with Torpenter (TOR) and end-state corrections (EC) based on mechanical embedding with ANI-2x. The error bars show the respective standard deviations. The experimental reference results are denoted with EXP. All data are in kcal mol<sup>-1</sup>.

Ligand A	Ligand B	EXP	OFF2.2.0	EC-OFF2.2.0	TOR	EC-TOR
18624	18626	-0.4	-0.8 ± 0.0	-0.9 ± 2	-0.7 ± 0.0	-0.5 ± 1.0
18624	18630	-0.65	-0.5 ± 0.1	-0.6 ± 1.6	-0.4 ± 0.1	-0.5 ± 0.8
18624	18633	-0.69	-0.7 ± 0.0	-1.0 ± 1.2	-0.8 ± 0.0	0.2 ± 0.9
18625	18628	-0.6	0.8 ± 0.1	2.6 ± 1.1	1.0 ± 0.1	1.5 ± 1.1
18625	18631	-1.32	-1.6 ± 0.3	-0.1 ± 1.5	-1.3 ± 0.3	0.2 ± 1.5
18626	18627	0.39	0.3 ± 0.1	0.1 ± 2.5	0.3 ± 0.1	-0.4 ± 0.9
18626	18629	0.19	0.3 ± 0.2	0.9 ± 2.7	0.4 ± 0.2	1.1 ± 1.1
18626	18632	-0.22	-0.2 ± 0.3	-0.1 ± 2.1	-0.2 ± 0.3	0.9 ± 1
18627	18630	-0.66	0.0 ± 0.0	0.2 ± 2.2	0.0 ± 0.0	0.4 ± 0.7
18627	18633	-0.7	-0.2 ± 0.0	-0.1 ± 2	-0.3 ± 0.0	1.2 ± 0.8
18628	18635	1.42	-0.6 ± 0.2	-1.5 ± 1.1	-0.7 ± 0.2	-0.3 ± 0.9
18629	18635	1.4	0.3 ± 0.4	-0.1 ± 2.1	0.6 ± 0.4	0.8 ± 1.1
18631	18634	-0.58	-0.8 ± 0.1	0.1 ± 1.8	-1.0 ± 0.1	-1.4 ± 1.5
18632	18634	-0.91	-1.9 ± 0.3	-0.4 ± 1.7	-1.4 ± 0.3	-1.4 ± 1.1
18634	18637	-0.15	-0.8 ± 0.2	-3 ± 1.3	-0.9 ± 0.2	0.8 ± 0.9
18634	18638	-0.1	0.0 ± 0.2	-0.1 ± 2.6	0.0 ± 0.2	-1.0 ± 0.9
18634	18652	-0.69	-0.3 ± 0.5	-0.1 ± 1.9	-1.0 ± 0.5	-1.4 ± 1.7
18634	18658	0.3	0.3 ± 0.2	-1.5 ± 1.2	0.4 ± 0.2	0.2 ± 1.7
18634	18659	0.53	0.0 ± 0.3	-1.6 ± 1.8	-0.1 ± 0.3	-1.1 ± 0.9
18634	18660	1.3	0.6 ± 0.0	-0.9 ± 1.3	1.2 ± 0.0	0.7 ± 1.6
18637	18639	0.41	0.6 ± 0.3	1.6 ± 1.7	0.2 ± 0.3	-2.4 ± 1.1
18638	18639	0.36	-0.2 ± 0.3	-1.3 ± 2.8	-0.6 ± 0.3	-0.6 ± 1.1
18639	18652	-0.95	-0.1 ± 0.7	1.3 ± 2.3	-0.3 ± 0.7	0.3 ± 1.9
18639	18660	1.04	0.8 ± 0.3	0.6 ± 1.7	1.8 ± 0.3	2.3 ± 1.7
18658	18659	0.23	-0.3 ± 0.2	-0.1 ± 1.4	-0.5 ± 0.2	-1.3 ± 1.5

Table S5: P38 relative binding free energy results, based on MM simulations with Open Force Field (OFF2.2.0), reparameterized torsion potentials with Torpenter (TOR) and end-state corrections (EC) based on mechanical embedding with ANI-2x. The error bars show the respective standard deviations. The experimental reference results are denoted with EXP. All data are in kcal mol<sup>-1</sup>.

Ligand A	Ligand B	EXP	OFF2.2.0	EC-OFF2.2.0	TOR	EC-TOR
2aa	2z	-1.1	0.2 ± 0.2	0.1 ± 0.6	0.1 ± 0.3	-0.2 ± 0.7
2aa	3flq	-0.7	1.2 ± 0.8	1.5 ± 1.2	-1.1 ± 0.7	0.4 ± 1.0
2aa	3flw	-1.4	-0.7 ± 0.7	0.1 ± 1.0	-2.2 ± 0.8	-1.9 ± 1.2
2aa	3fmh	-1.6	-0.5 ± 0.4	-0.6 ± 0.8	-1.9 ± 0.7	-1.2 ± 0.9
2aa	3fmk	-2.6	-2.9 ± 0.3	-1.3 ± 0.7	-3.6 ± 0.3	-2.3 ± 0.6
2bb	2v	0.1	0.7 ± 0.5	0.7 ± 1.2	2.1 ± 0.3	1.1 ± 0.8
2bb	2y	-0.7	-1.5 ± 0.7	-1.9 ± 1.3	-0.3 ± 0.3	-1.9 ± 0.8
2c	2h	1.0	2.1 ± 0.7	0.2 ± 0.8	2.1 ± 1.3	0.9 ± 1.3
2c	2i	0.4	1.8 ± 0.7	0.7 ± 0.8	1.4 ± 1.1	0.8 ± 1.1
2e	3fn	-0.2	-0.8 ± 0.1	-1.1 ± 0.2	-1.2 ± 0.2	-1.0 ± 0.5
2e	3flz	1.2	0.1 ± 0.3	0.4 ± 0.4	-0.1 ± 0.0	0.4 ± 0.3
2ee	2j	2.2	1.2 ± 0.4	2.4 ± 0.6	1.8 ± 0.2	0.6 ± 0.3
2ee	3fn	1.4	0.1 ± 0.1	0.2 ± 0.3	-0.1 ± 0.2	-1.4 ± 0.5
2f	2g	-2.2	-0.5 ± 0.2	-1.1 ± 0.2	-0.6 ± 0.0	-0.6 ± 0.6
2f	3flz	-1.0	0.2 ± 0.3	-0.4 ± 0.4	0.4 ± 0.1	0.4 ± 0.6
2ff	2j	1.4	1.0 ± 0.4	2.2 ± 0.6	1.5 ± 0.3	1.3 ± 0.7
2ff	3fn	0.6	0.0 ± 0.1	0.1 ± 0.3	-0.4 ± 0.1	-0.7 ± 0.7
2g	3fn	-0.2	-0.1 ± 0.1	-0.6 ± 0.2	-0.1 ± 0.2	-0.3 ± 0.4
2gg	2m	-0.3	-2.6 ± 0.2	-2.6 ± 0.6	-2.6 ± 0.3	-3.2 ± 0.4
2gg	2n	-1.2	-1.8 ± 0.4	-1.0 ± 0.7	-0.5 ± 0.2	0.1 ± 0.6
2gg	2o	0.2	-0.3 ± 0.3	0.8 ± 0.9	-0.5 ± 0.3	0.4 ± 0.5
2gg	2r	-0.1	-1.9 ± 0.1	-2.1 ± 1.0	-1.8 ± 0.8	-1.8 ± 1.0
2gg	2s	-0.4	-1.6 ± 0.4	-0.5 ± 0.8	-1.1 ± 0.3	-0.4 ± 0.5
2gg	2u	-1.6	-3.4 ± 0.3	-2.2 ± 0.7	-3.4 ± 0.5	-2.8 ± 0.7
2gg	2v	1.7	1.8 ± 0.2	3.1 ± 0.6	2.2 ± 0.1	2.9 ± 0.3
2h	2i	-0.6	-0.3 ± 0.4	0.5 ± 0.5	-0.7 ± 0.2	-0.1 ± 0.3
2h	2m	-1.5	-3.7 ± 0.3	-4.0 ± 0.5	-4.2 ± 0.3	-4.7 ± 0.3
2h	2o	-1.0	-1.5 ± 0.4	-0.8 ± 0.8	-2.1 ± 0.5	-1.0 ± 0.6
2h	2r	-1.3	-3.1 ± 0.5	-3.6 ± 1.0	-3.4 ± 0.8	-3.2 ± 1.0
2h	2u	-2.8	-4.5 ± 0.5	-3.7 ± 0.7	-5.0 ± 0.4	-4.3 ± 0.6
2h	2v	0.5	0.7 ± 0.4	1.6 ± 0.5	0.6 ± 0.4	1.4 ± 0.5
2j	2v	1.1	-0.2 ± 0.1	-0.5 ± 0.4	-0.9 ± 0.2	0.3 ± 0.3
2k	2t	-1.3	-3.0 ± 0.3	-3.5 ± 0.5	-2.9 ± 0.1	-3.4 ± 0.4
2k	3fn	-0.3	-0.9 ± 0.3	-1.0 ± 0.4	-0.6 ± 0.1	-1.0 ± 0.4
2l	2p	1.1	-0.4 ± 0.5	-0.3 ± 0.8	-0.7 ± 0.2	-1.0 ± 0.3
2l	2q	0.0	-1.5 ± 0.5	-0.6 ± 0.6	-1.0 ± 0.3	-0.9 ± 0.4
2n	2s	0.7	0.2 ± 0.8	0.5 ± 0.9	-0.6 ± 0.5	-0.5 ± 0.8
2p	2x	1.0	0.5 ± 0.8	0.9 ± 1.1	1.3 ± 2.1	1.4 ± 1.4
2q	2x	2.0	1.5 ± 1.6	1.1 ± 1.7	1.5 ± 2.1	1.6 ± 1.6
2t	3fn	1.0	2.1 ± 0.4	2.5 ± 0.6	2.3 ± 0.1	2.4 ± 0.5
2v	2x	-1.3	-1.5 ± 0.2	-2.6 ± 0.7	-1.3 ± 0.2	-1.8 ± 0.5
2v	2y	-0.8	-2.2 ± 0.2	-2.6 ± 0.4	-2.4 ± 0.1	-3.0 ± 0.3
2v	3fn	-1.9	-0.9 ± 0.2	-1.7 ± 0.3	-1.1 ± 0.2	-2.4 ± 0.5
2v	3fly	-2.4	-1.7 ± 0.2	-2.2 ± 0.3	-1.9 ± 0.2	-2.2 ± 0.3
2x	3fly	-1.2	-0.2 ± 0.2	0.5 ± 0.7	-0.6 ± 0.1	-0.4 ± 0.5
2z	3fly	-1.1	-0.4 ± 0.6	0.1 ± 0.6	-1.0 ± 0.6	-0.1 ± 0.7
3flq	3fly	-1.5	-1.4 ± 0.7	-1.4 ± 1.0	0.2 ± 0.2	-0.7 ± 0.6
3flw	3fly	-0.7	0.9 ± 0.5	0.5 ± 0.6	1.4 ± 1.1	1.7 ± 1.3
3fly	3fmh	0.6	-0.3 ± 0.1	-0.7 ± 0.4	-1.0 ± 0.3	-0.9 ± 0.4
3fly	3fmk	-0.4	-2.7 ± 0.5	-1.4 ± 0.5	-2.7 ± 1.2	-2.0 ± 1.2

Table S6: End-state correction (EC) results and the corresponding standard deviations (STD) from three independent runs for the **TYK2** system using both the Open force field 2.2.0 (OFF2.2.0) and Torpenter (TOR).

Ligand	EC-OFF2.2.0	STD-OFF2.2.0	EC-TOR	STD-TOR
ejm_31	3.3	0.9	1.1	0.9
ejm_42	2.2	0.4	1.6	0.5
ejm_43	2.3	0.6	1.8	0.4
ejm_44	1.7	0.4	1.3	0.3
ejm_45	2.4	0.4	2.0	0.1
ejm_46	1.2	0.3	1.4	0.5
ejm_47	2.4	0.4	1.5	0.5
ejm_48	2.4	0.7	1.1	0.6
ejm_49	2.6	0.7	2.9	0.2
ejm_50	2.4	0.6	2.2	0.3
ejm_54	2.0	0.5	1.3	0.1
ejm_55	2.7	0.6	0.4	0.0
jmc_23	1.9	0.7	1.8	0.6
jmc_27	1.6	0.5	1.3	0.4
jmc_28	1.5	0.5	1.9	0.1
jmc_30	2.3	0.7	2.4	0.2
average		0.6		0.4

Table S7: End-state correction (EC) results and the corresponding standard deviations (STD) from three independent runs for the **CDK2** system using both the Open force field 2.2.0 (OFF2.2.0) and Torpenter (TOR).

Ligand	EC-OFF2.2.0	STD-OFF2.2.0	EC-TOR	STD-TOR
1h1q	-2.0	0.5	-1.7	0.1
1h1r	-1.1	0.2	-0.8	0.1
1h1s	-2.2	0.7	-1.8	0.4
1oi9	-1.6	0.0	-1.6	0.4
1oiu	0.0	0.6	0.4	0.7
1oiy	-2.2	0.1	-1.3	0.1
20	-1.7	0.6	-0.7	0.3
21	-1.5	0.1	-1.4	0.2
22	-0.6	0.2	-1.1	0.1
26	-1.6	0.0	-1.5	0.3
28	-2.1	0.1	-2.0	0.3
29	-1.4	0.1	-1.3	0.3
30	-1.2	0.0	-1.0	0.2
31	-1.6	0.1	-1.6	0.1
32	-0.9	0.0	-2.7	0.4
average		0.2		0.3

Table S8: End-state correction (EC) results and the corresponding standard deviations (STD) from three independent runs for the **JNK1** system using both the Open force field 2.2.0 (OFF2.2.0) and Torpenter (TOR).

Ligand	EC-OFF2.2.0	STD-OFF2.2.0	EC-TOR	STD-TOR
18624	2.3	1.1	2.6	0.8
18625	1.4	0.4	2.8	0.7
18626	2.1	1.7	2.8	0.6
18627	2.0	1.9	2.2	0.6
18628	3.3	1.0	3.4	0.8
18629	2.7	2.1	3.6	0.8
18630	2.1	1.1	2.6	0.3
18631	2.9	1.4	4.3	1.3
18632	2.3	1.2	3.9	0.7
18633	2.0	0.6	3.6	0.5
18634	3.8	1.1	4.0	0.8
18635	2.3	0.1	3.8	0.5
18637	1.6	0.6	5.6	0.3
18638	3.7	2.3	3.0	0.3
18639	2.6	1.6	3.0	1.0
18652	4.0	1.5	3.6	1.4
18658	2.0	0.2	3.8	1.5
18659	2.2	1.3	3.0	0.3
18660	2.4	0.7	3.5	1.3
average		1.2		0.8

Table S9: End-state correction (EC) results and the corresponding standard deviations (STD) from three independent runs for the **P38** system using both the Open force field 2.2.0 (OFF2.2.0) and Torpenter (TOR).

Ligand	EC-OFF2.2.0	STD-OFF2.2.0	EC-TOR	STD-TOR
2aa	-2.1	0.6	-1.5	0.5
2bb	-1.3	1.0	0.4	0.7
2c	-0.2	0.3	-0.2	0.2
2e	-1.8	0.1	-2.0	0.2
2ee	-2.1	0.2	-0.6	0.3
2f	-0.9	0.1	-1.4	0.4
2ff	-2.1	0.3	-1.6	0.6
2g	-1.5	0.1	-1.6	0.1
2gg	-2.5	0.5	-1.3	0.2
2h	-2.1	0.3	-1.4	0.1
2i	-1.3	0.1	-0.8	0.1
2j	-1.0	0.4	-1.8	0.1
2k	-1.9	0.2	-1.4	0.2
2l	-2.9	0.3	-2.0	0.2
2m	-2.5	0.3	-1.9	0.1
2n	-1.7	0.2	-0.7	0.5
2o	-1.4	0.7	-0.3	0.3
2p	-2.8	0.5	-2.3	0.1
2q	-2.0	0.1	-1.9	0.2
2r	-2.7	0.9	-1.2	0.6
2s	-1.4	0.4	-0.5	0.3
2t	-2.4	0.4	-1.9	0.3
2u	-1.3	0.3	-0.7	0.4
2v	-1.3	0.1	-0.6	0.2
2x	-2.4	0.6	-1.1	0.4
2y	-1.6	0.3	-1.2	0.1
2z	-2.2	0.2	-1.8	0.4
3fn	-2.0	0.1	-1.9	0.4
3flq	-1.8	0.7	0.0	0.5
3flw	-1.3	0.3	-1.2	0.8
3fly	-1.7	0.1	-0.9	0.1
3flz	-1.5	0.2	-1.6	0.2
3fmh	-2.2	0.4	-0.8	0.3
3fmk	-0.5	0.1	-0.3	0.0
average		0.3		0.3



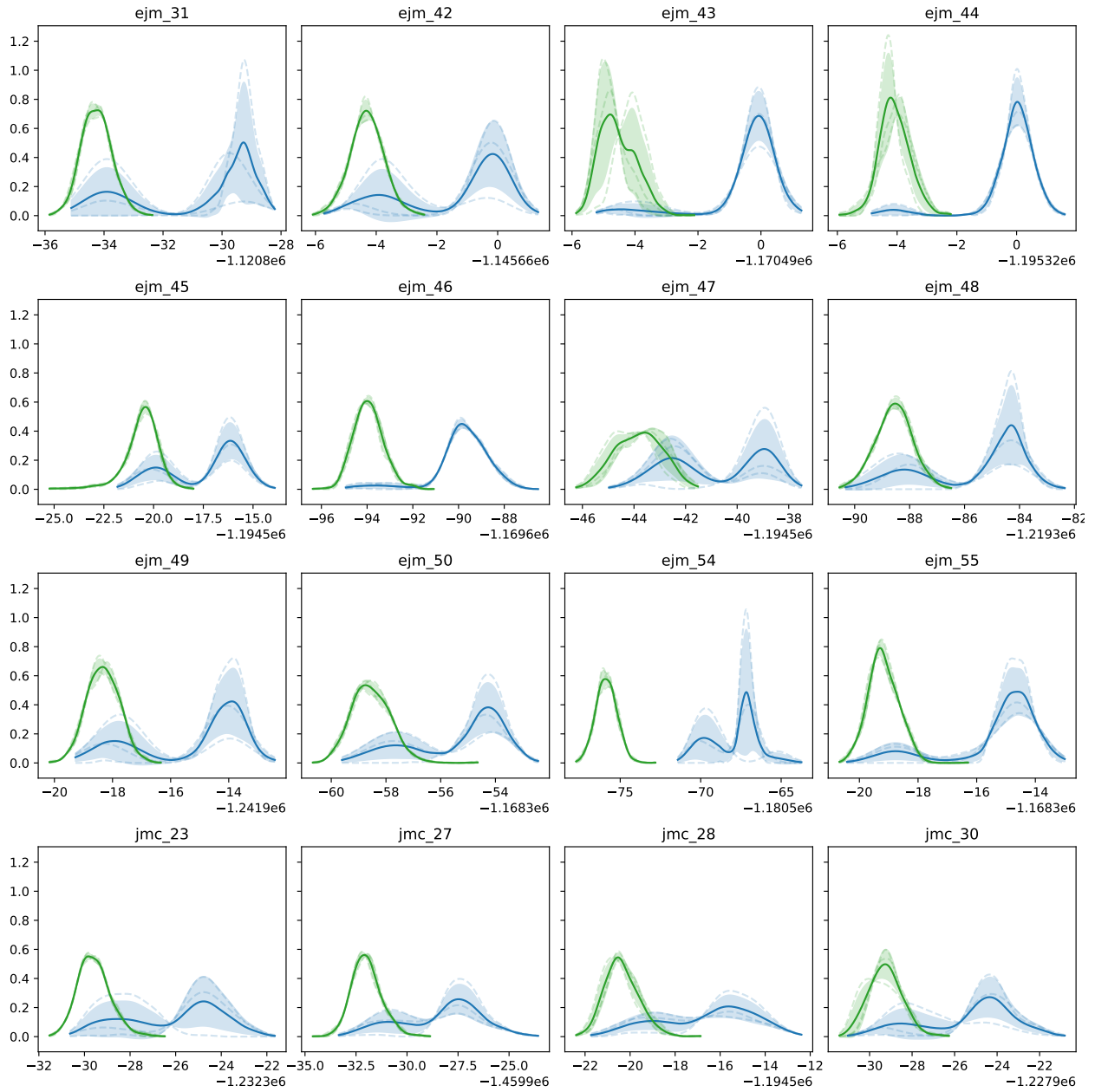


**Figure S1.** Kernel density plots for the work values of the 300 switches are presented for the **TYK2-OFF** system in the free leg. Blue indicates the forward direction, switching from MM to ML, while green represents the backward direction (ML to MM). The dashed lines display the density plot for each repeat, whereas the solid blue or green lines represent the average across the three independent runs. The shaded blue and green areas illustrate the standard deviation between the three runs at each point either for the forward (blue) or backwards (green) direction.

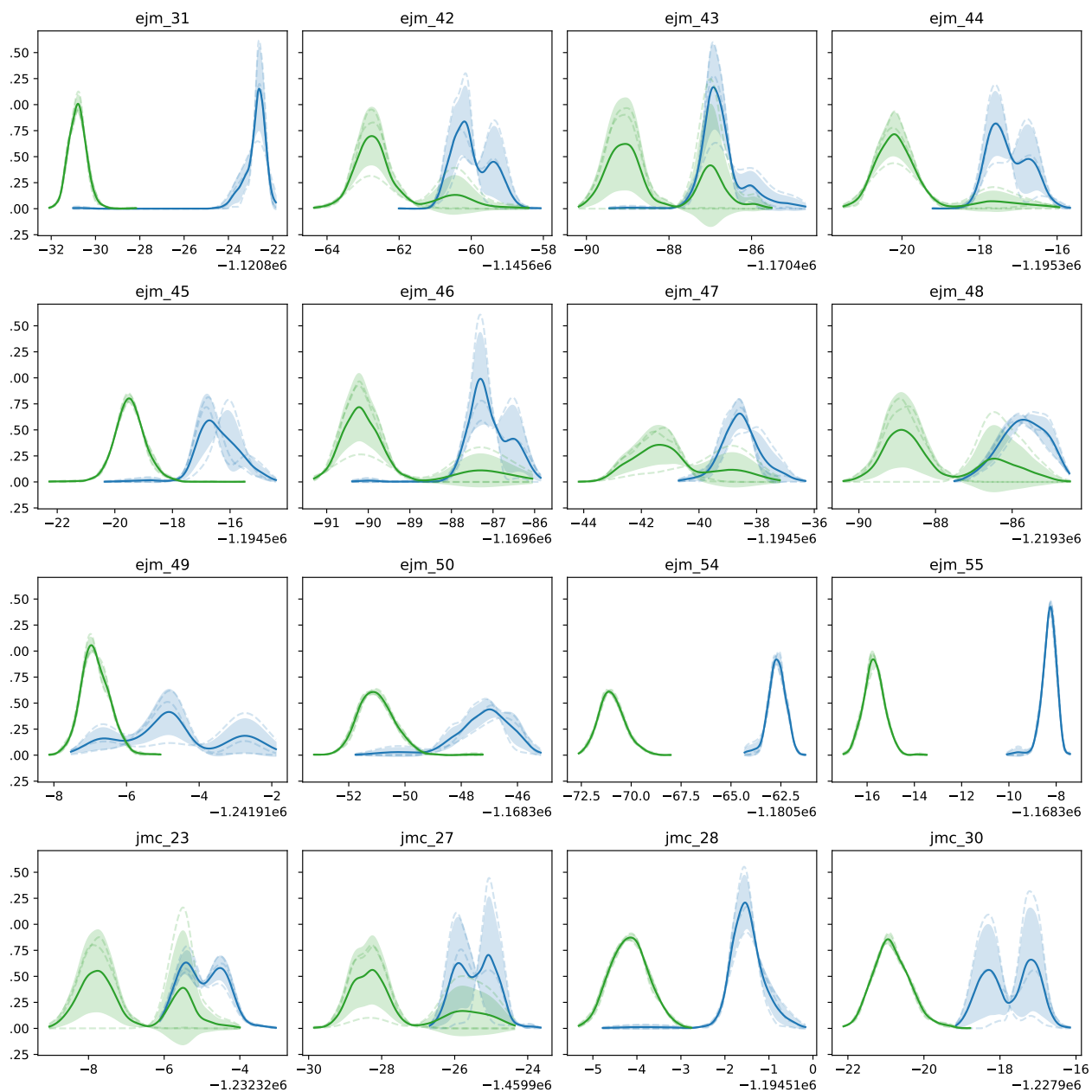


**Figure S2.** Kernel density plots for the work values of the 300 switches are presented for the **TYK2-TOR** system in the free leg. Blue indicates the forward direction, switching from MM to ML, while green represents the backward direction (ML to MM). The dashed lines display the density plot for each repeat, whereas the solid blue or green lines represent the average across the three independent runs. The shaded blue and green areas illustrate the standard deviation between the three runs at each point either for the forward (blue) or backwards (green) direction.

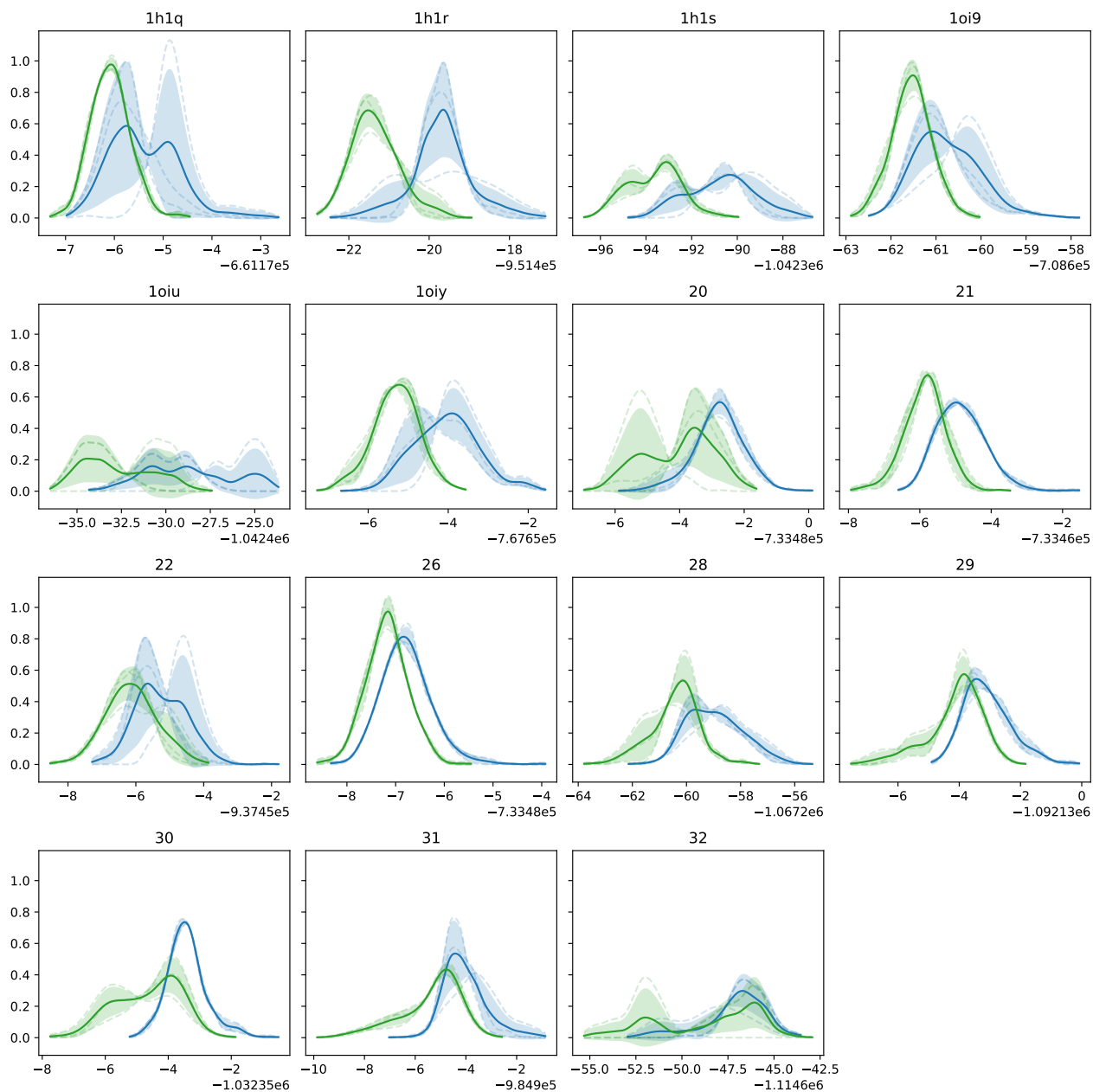


**Figure S3.** Kernel density plots for the work values of the 300 switches are presented for the **CDK2-OFF2.2.0** system in the free leg. Blue indicates the forward direction, switching from MM to ML, while green represents the backward direction (ML to MM). The dashed lines display the density plot for each repeat, whereas the solid blue or green lines represent the average across the three independent runs. The shaded blue and green areas illustrate the standard deviation between the three runs at each point either for the forward (blue) or backwards (green) direction.

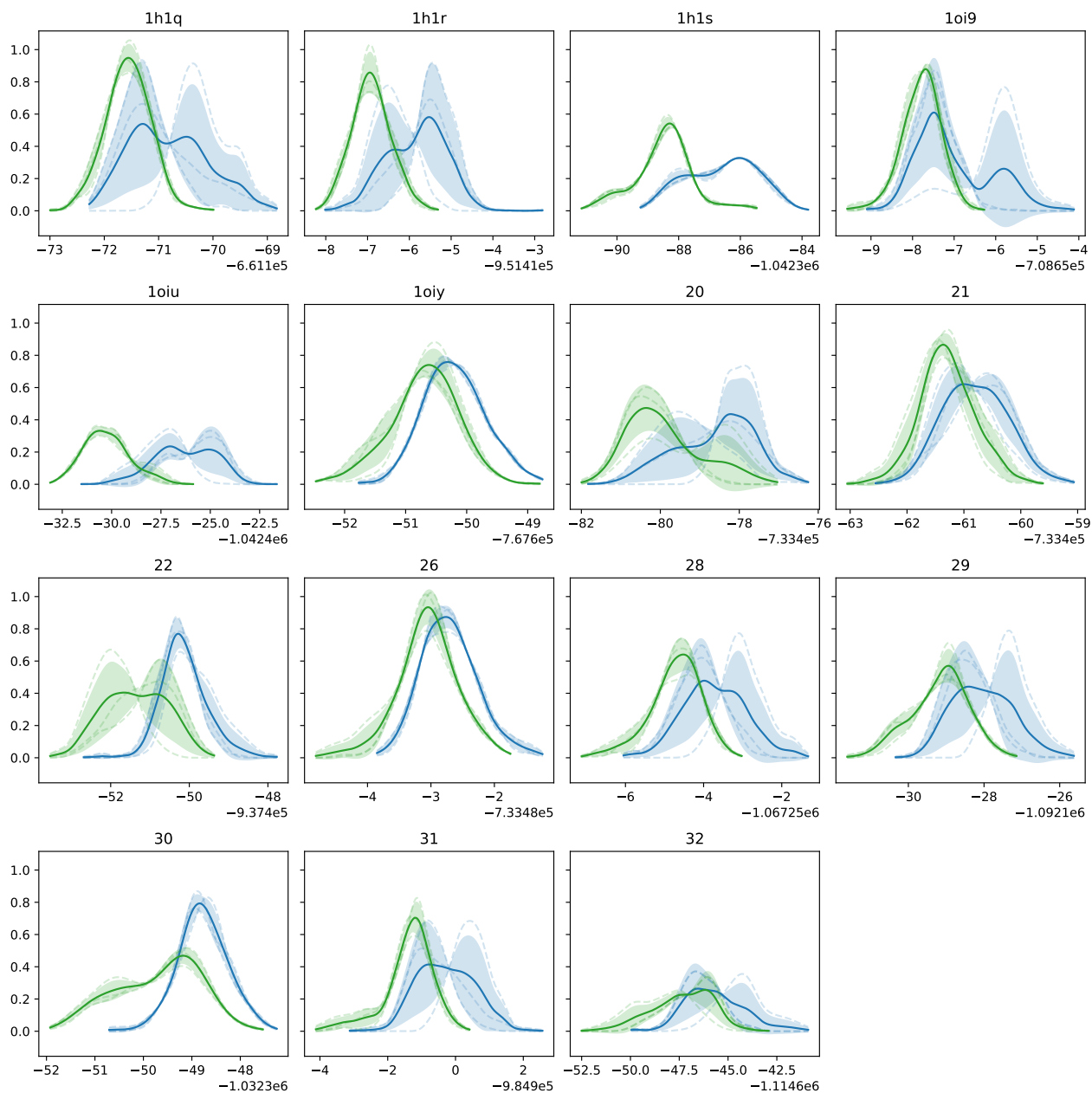


**Figure S4.** Kernel density plots for the work values of the 300 switches are presented for the **CDK2-TOR** system in the free leg. Blue indicates the forward direction, switching from MM to ML, while green represents the backward direction (ML to MM). The dashed lines display the density plot for each repeat, whereas the solid blue or green lines represent the average across the three independent runs. The shaded blue and green areas illustrate the standard deviation between the three runs at each point either for the forward (blue) or backwards (green) direction.



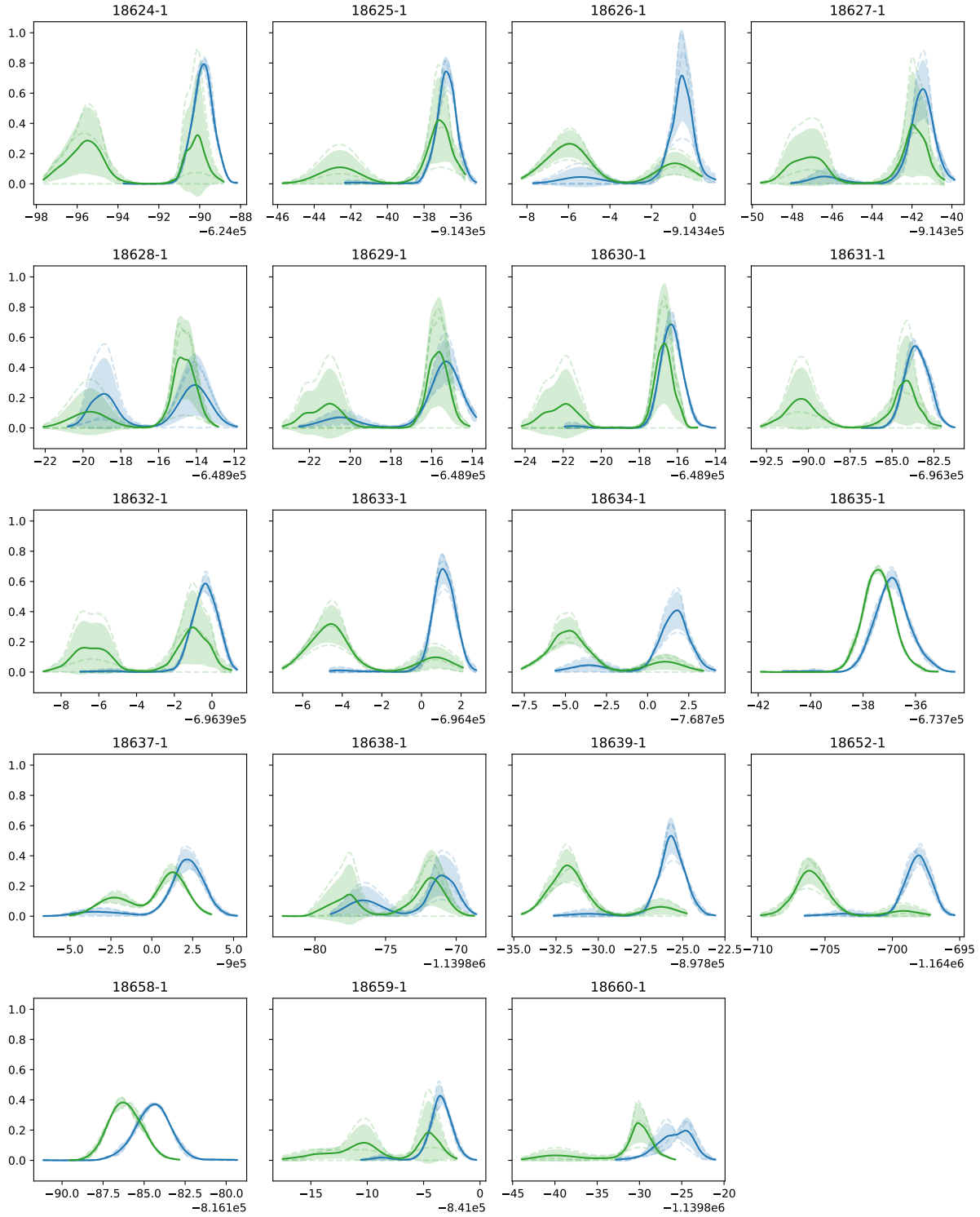


**Figure S5.** Kernel density plots for the work values of the 300 switches are presented for the **JNK1-OFF2.2.0** system in the free leg. Blue indicates the forward direction, switching from MM to ML, while green represents the backward direction (ML to MM). The dashed lines display the density plot for each repeat, whereas the solid blue or green lines represent the average across the three independent runs. The shaded blue and green areas illustrate the standard deviation between the three runs at each point either for the forward (blue) or backwards (green) direction.



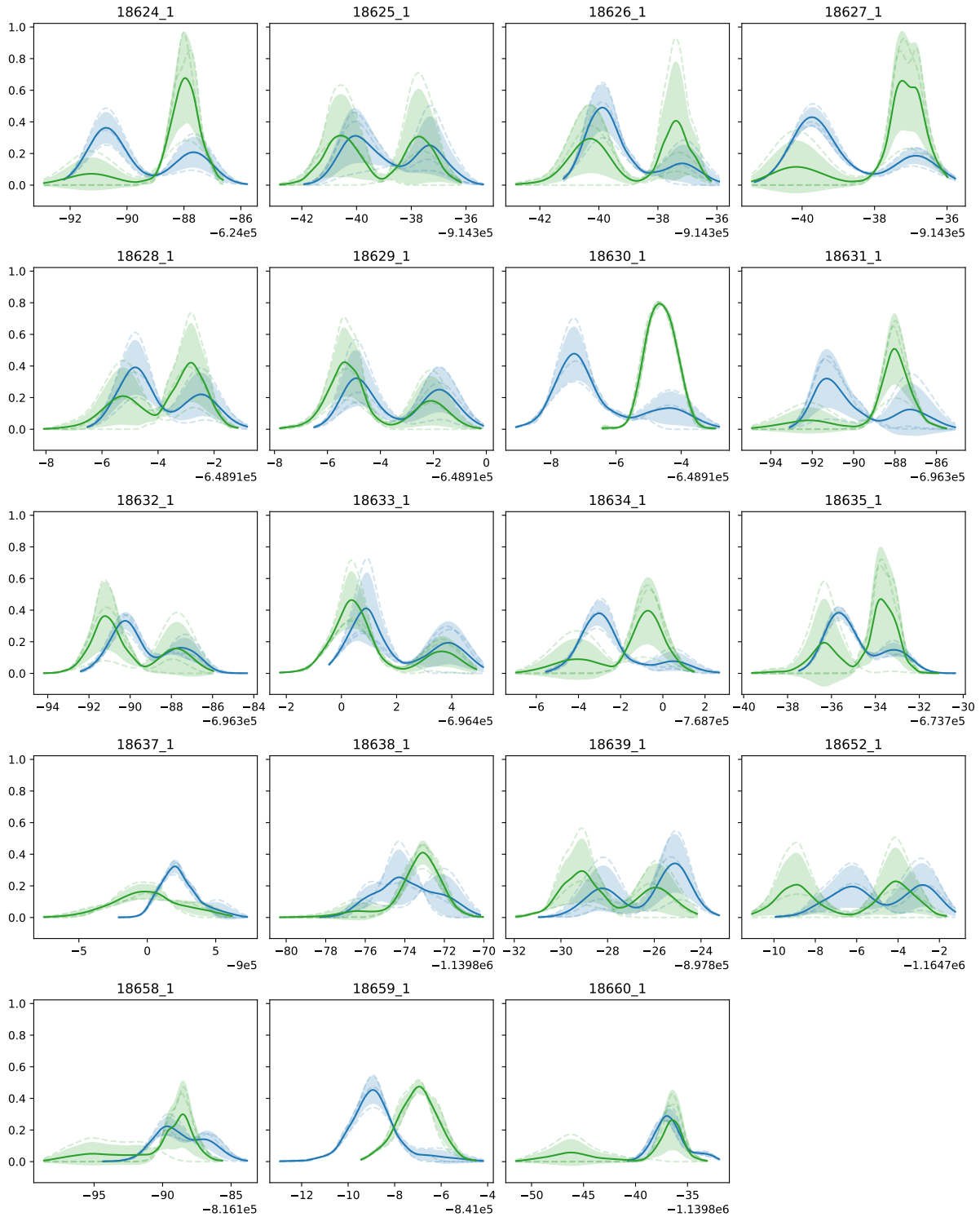


**Figure S6.** Kernel density plots for the work values of the 300 switches are presented for the **JNK1-TOR** system in the free leg. Blue indicates the forward direction, switching from MM to ML, while green represents the backward direction (ML to MM). The dashed lines display the density plot for each repeat, whereas the solid blue or green lines represent the average across the three independent runs. The shaded blue and green areas illustrate the standard deviation between the three runs at each point either for the forward (blue) or backwards (green) direction.



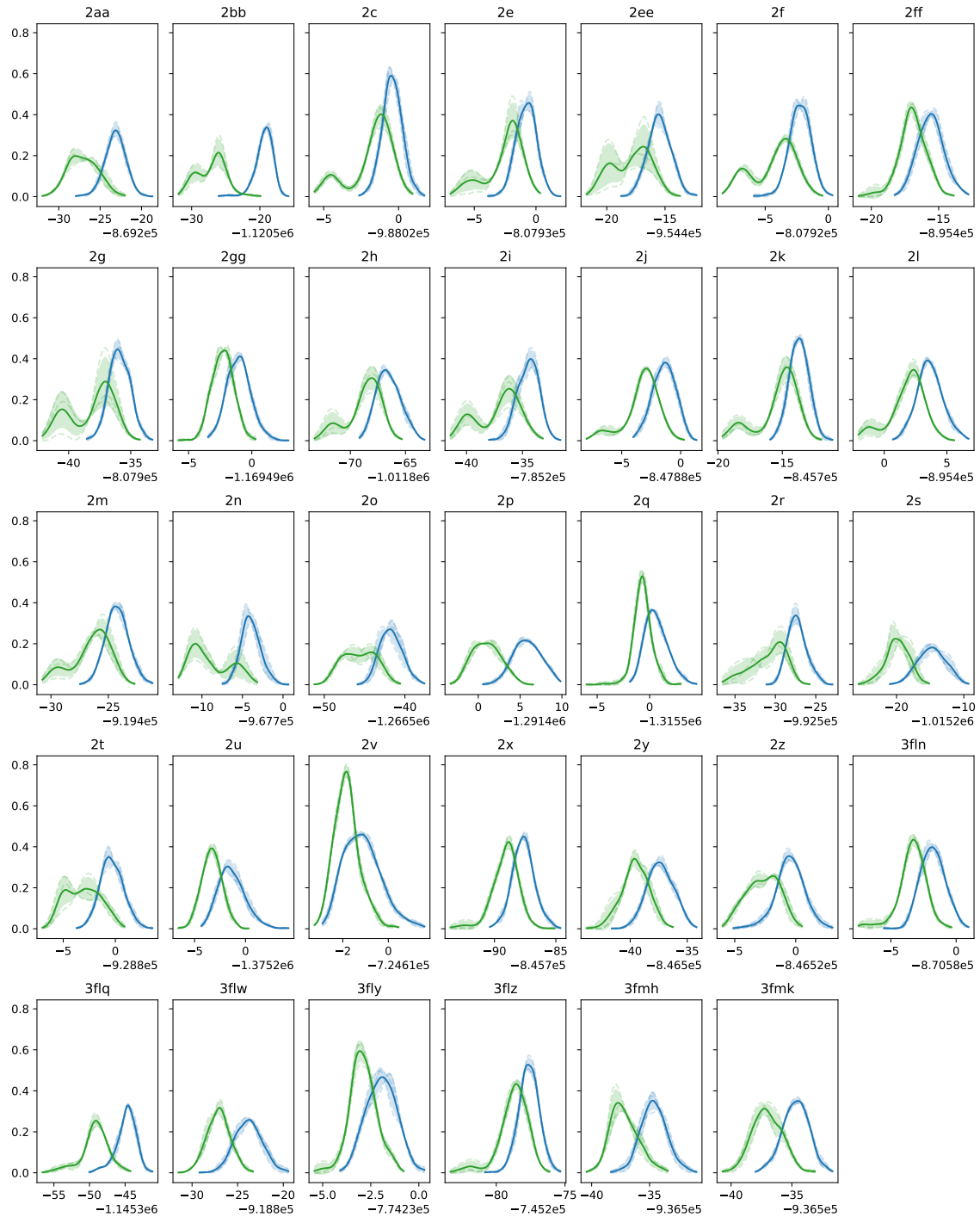


**Figure S7.** Kernel density plots for the work values of the 300 switches are presented for the **P38-OFF** system in the free leg. Blue indicates the forward direction, switching from MM to ML, while green represents the backward direction (ML to MM). The dashed lines display the density plot for each repeat, whereas the solid blue or green lines represent the average across the three independent runs. The shaded blue and green areas illustrate the standard deviation between the three runs at each point either for the forward (blue) or backwards (green) direction.



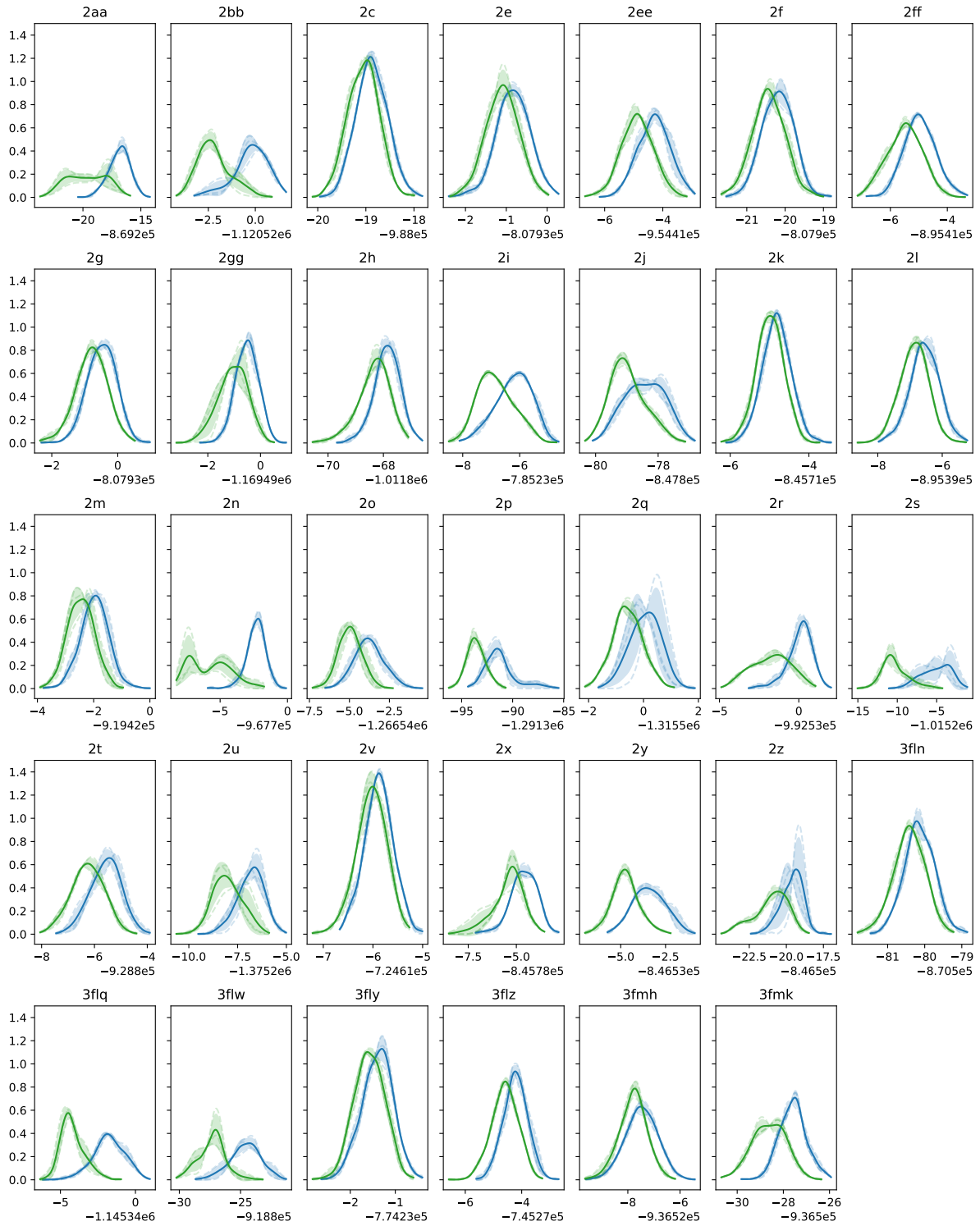


**Figure S8.** Kernel density plots for the work values of the 300 switches are presented for the **P38-TOR** system in the free leg. Blue indicates the forward direction, switching from MM to ML, while green represents the backward direction (ML to MM). The dashed lines display the density plot for each repeat, whereas the solid blue or green lines represent the average across the three independent runs. The shaded blue and green areas illustrate the standard deviation between the three runs at each point either for the forward (blue) or backwards (green) direction.

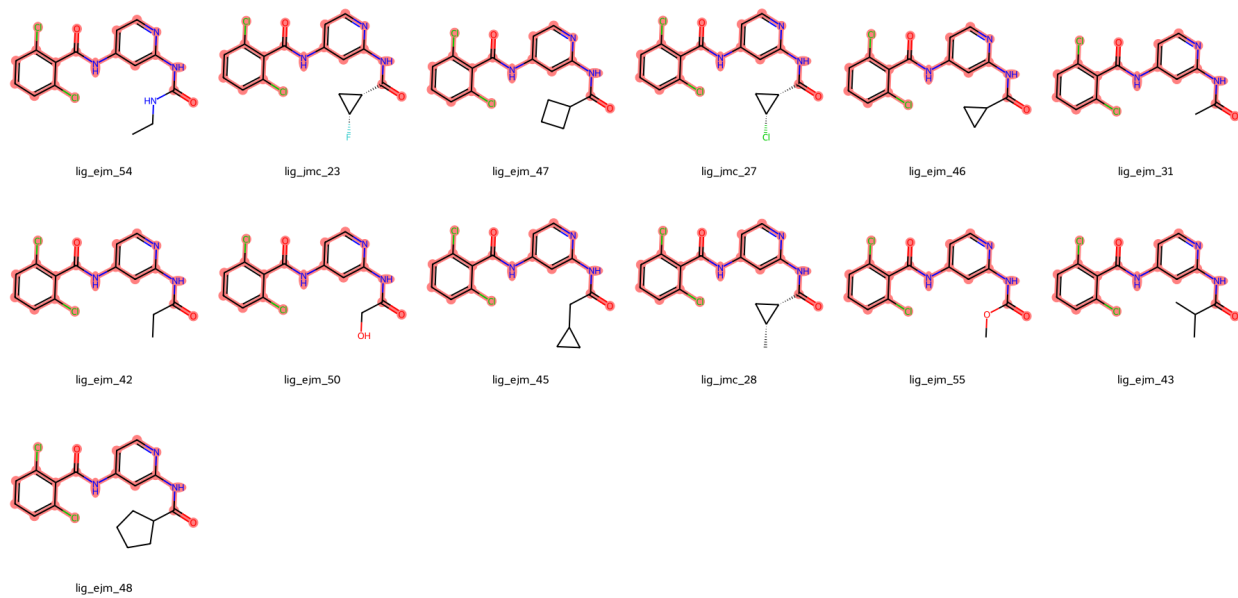


**Figure S9.** Ligands used in the TYK2 set. The common substructure is highlighted in orange.

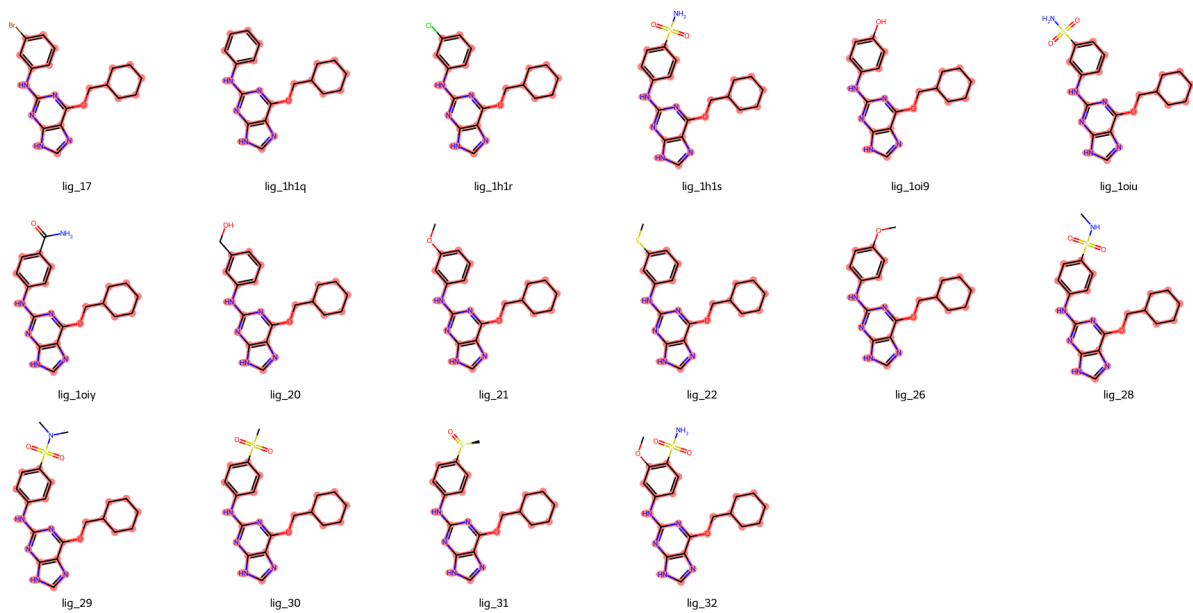


**Figure S10.** Ligands used in the CDK2 set. The common substructure is highlighted in orange. Ligand 17 had to be excluded because its Br group is incompatible with the ANI-2x ML potential.

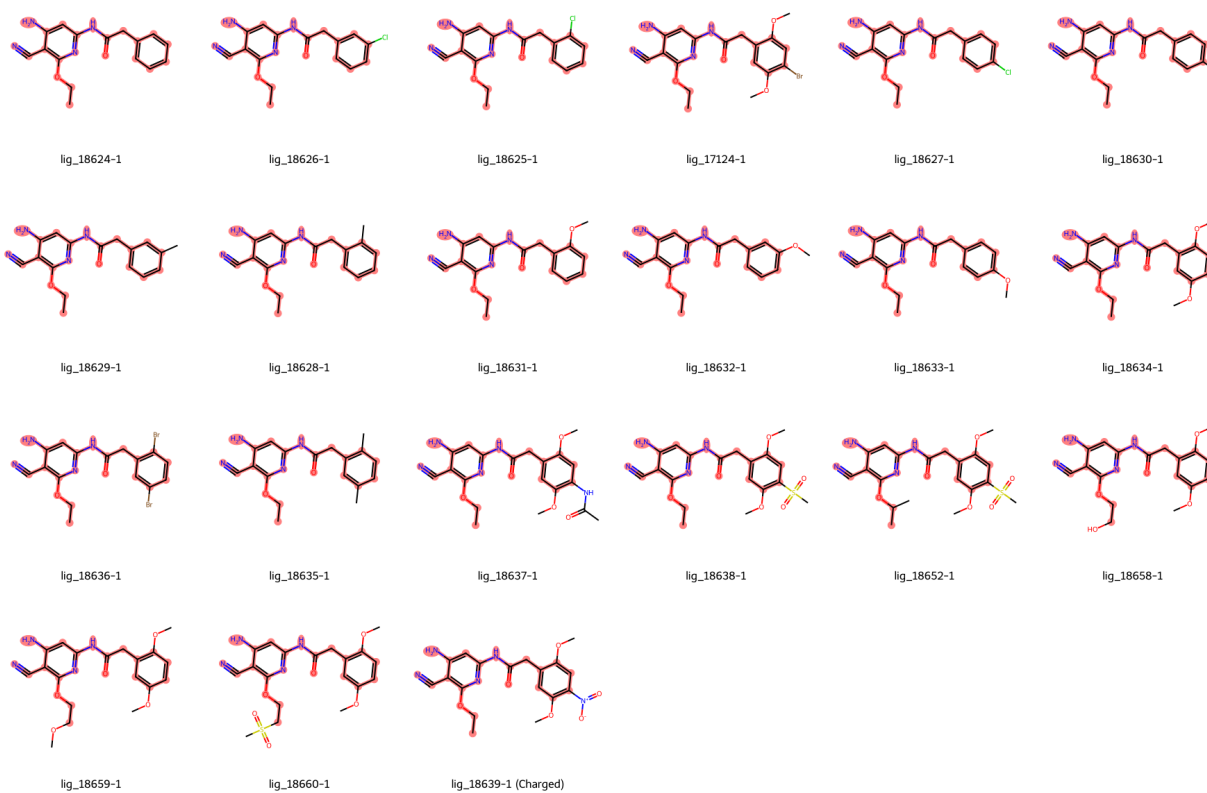


**Figure S11.** Ligands used in the JNK1 set. The common substructure is highlighted in orange. Ligands 18624 and 18636 had to be excluded because the ANI-2x ML potential does not contain parameters for Br. Ligand 18639 had to be excluded because its charged group is incompatible with the ANI-2x ML potential.



**Figure S12.** Ligands used in the P38 set. The common substructure is highlighted in orange.